

1 The Great Balls of Fire: A probabilistic approach to  
2 quantify the hazard related to ballistics — a case study  
3 at La Fossa volcano, Vulcano Island, Italy

4 Sebastien Biass<sup>a,b</sup>, Jean-Luc Falcone<sup>c</sup>, Costanza Bonadonna<sup>a</sup>, Federico Di  
5 Traglia<sup>d</sup>, Marco Pistolesi<sup>d</sup>, Mauro Rosi<sup>d</sup>, Pierino Lestuzzi<sup>e</sup>

6 <sup>a</sup>*Department of Earth Sciences, University of Geneva, Switzerland*

7 <sup>b</sup>*Department of Geology and Geophysics, University of Hawai'i at Manoa, USA*

8 <sup>c</sup>*Department of Computing Sciences, University of Geneva, CUI, Batelle - Batiment A,  
9 7, route de Drize, CH-1227 Carouge, Switzerland*

10 <sup>d</sup>*Dipartimento di Scienze della Terra, Università di Pisa, Pisa, Italy*

11 <sup>e</sup>*Ecole Polytechnique Fédérale de Lausanne, ENAC IIC IMAC, Lausanne, Switzerland*

---

12 **Abstract**

13 We present a probabilistic approach to quantify the hazard posed by  
14 volcanic ballistic projectiles (VBP) and their potential impact on the built  
15 environment. A model named *The Great Balls of Fire* (GBF) is introduced to  
16 describe ballistic trajectories of VBPs accounting for variable drag coefficients  
17 and topography. It relies on a few key input parameters easily identifiable in  
18 the field and is designed to model large numbers of VBPs stochastically. As-  
19 sociated functions come with the GBF code to post-process model outputs  
20 into a comprehensive probabilistic hazard assessment for VBP impacts. Out-  
21 comes include probability maps to exceed given thresholds of kinetic energies  
22 at impact, hazard curves and probabilistic isoenergy maps. Probabilities are  
23 calculated either on equally-sized pixels or zones of interest.

24 The approach is calibrated, validated and applied to La Fossa volcano,  
25 the active crater of Vulcano Island (Italy). We constructed a generic eruption  
26 scenario based on stratigraphic studies and numerical inversions of the 1888–  
27 1890 long-lasting Vulcanian cycle of La Fossa. Results suggest a  $\sim 10^{-2}\%$   
28 probability of occurrence of VBP impacts with kinetic energies  $\leq 10^4$  J at  
29 the touristic locality of Porto. In parallel, the vulnerability to roof perfora-  
30 tion was estimated by combining field observations and published literature,  
31 allowing a first estimate of the potential impact of VBPs during future Vul-  
32 canian eruptions. Results indicate a high physical vulnerability to the VBP

33 hazard, and, consequently, half of the building stock having a  $\geq 2.5 \times 10^{-3}\%$   
34 probability of roof perforation.

35 *Keywords:* Probabilistic hazard assessment, Volcanic ballistic projectiles,  
36 Pre-event impact assessment, Physical vulnerability, Vulcano Island, La  
37 Fossa

---

## 38 1. Introduction

39 Volcanic ballistic projectiles (VBP) decouple from the jet phase of ex-  
40 plosive events to follow a near-ballistic trajectory modified by drag forces  
41 (Alatorre-Ibargüengoitia et al., 2012). VBPs can be distinguished between  
42 blocks, typically of angular shape and lithic origin, and bombs, typically of  
43 rounded shape and juvenile origin. These ballistic projectiles can be pro-  
44 duced in all types of volcanic eruptions, but are particularly abundant with  
45 Vulcanian, Strombolian and phreatic styles (e.g. Feeley and Winer, 2009;  
46 Vanderkluisen et al., 2012; Kaneko et al., 2016). VBPs constitute a major  
47 threat in proximal areas due to their high kinematic energies and tempera-  
48 tures that can impact life and the built environment and ignite fires. As ex-  
49 amples, Pomonis et al. (1999) reported VBPs  $<1$  kg penetrating thatched and  
50 galvanized iron roofs during previous eruptions of Furnas volcano (Azores),  
51 and Pistolesi et al. (2011) and Rosi et al. (2013) reported wildfires triggered  
52 by incandescent blocks during the 2007 crisis of Stromboli.

53 Numerous models for ballistic ejection have been developed since the  
54 1940's, primarily to invert field observations and estimate eruptive condi-  
55 tions (e.g. ejection velocity, i.e. Minakami, 1942; Fudali and Melson, 1971;  
56 Wilson, 1972; Steinberg and Lorenz, 1983). Although accounting for drag ef-  
57 fects, initial models considered the ejection of blocks into a still atmosphere,  
58 commonly leading to an overestimation of drag forces and, consequently, un-  
59 realistically high ejection velocities. In the context of Vulcanian eruptions,  
60 later models introduced a caprock accelerated by the gas expansion and be-  
61 having as a coherent plug until a maximum velocity is reached, at which  
62 point the fractured caprock disaggregates and individual ballistic blocks are  
63 released (Self et al., 1979; Wilson, 1980; Fagents and Wilson, 1993). This  
64 disaggregation height has been recently suggested to occur when the acceler-  
65 ation is 8% of the initial acceleration of the caprock (Alatorre-Ibargüengoitia  
66 et al., 2012). This implies a region of reduced drag in the vicinity of the  
67 eruptive source, within which the surrounding air moves radially from the

68 source at a velocity comparable to that of the clasts (Fagents and Wilson,  
69 1993). Using this concept, the effect of drag becomes important only when  
70 the velocity of the clast gradually decouples from that of the surrounding air,  
71 which allows to reproduce observed deposits with significantly lower ejection  
72 velocities.

73 Amongst all models, *Eject!* (Mastin, 2001) accounts for a region of re-  
74 duced drag (defined as a radius above the vent) and a variable drag coefficient  
75 and to describe the ballistic motion as a function of input parameters (e.g.  
76 block density, ejection velocity and angle). De' Michieli Vitturi et al. (2010)  
77 proposed a coupled Eulerian-Lagrangian model to describe the dynamics of  
78 large particles during Vulcanian eruptions, providing a detailed parametriza-  
79 tion of the complex radial and vertical acceleration and deceleration patterns  
80 of the initial jet phase. Alatorre-Ibargüengoitia et al. (2012) presented a  
81 model coupling lab measurements of the effect of shape on the drag of volcanic  
82 particles and a caprock model relating the energy consumption required by  
83 fragmentation to the ejection velocity of ballistics (Alatorre-Ibargüengoitia  
84 and Delgado-Granados, 2006; Alatorre-Ibargüengoitia et al., 2010). Recently,  
85 Tsunematsu et al. (2014) developed a new approach accounting for multiple  
86 particles and collision between bombs.

87 The aim of hazard assessments is to quantify the geographical and tem-  
88 poral probabilities of occurrence of a hazardous phenomenon of a given mag-  
89 nitude (Fournier d'Albe, 1979; Mendoza-Rosas and De la Cruz-Reyna, 2008).  
90 In volcanology, where eruptions constitute a multi-hazard system, this pro-  
91 cess is commonly achieved by i) the field characterization of the deposits in  
92 order to constrain and quantify eruption source parameters (ESPs), ii) the  
93 compilation of a catalogue of eruptions and phenomena at a given volcano  
94 to infer eruption scenarios and iii) the forward modelling of a given phe-  
95 nomenon using appropriate models (e.g. Biass et al., 2014). Recent hazard  
96 assessments in all fields of natural hazards increasingly rely upon probabilis-  
97 tic techniques in order to account for the inherent uncertainty of natural  
98 processes (e.g. Geist and Parsons, 2006; Gonzalez et al., 2009; Heneka and  
99 Hofherr, 2011). In volcanology, stochastic strategies have been widely applied  
100 to the modelling of tephra (e.g. Bonadonna, 2006; Jenkins et al., 2012) and,  
101 more recently, lava flows (e.g. Connor et al., 2012), for which probabilistic  
102 eruption scenarios are characterized by relevant ESPs defined as probability  
103 distributions. Hazard assessments for ballistics are, however, often based on  
104 a deterministic definition of eruption scenarios aiming at producing hazard  
105 zones for different block size, ejection angle and initial velocities (Alatorre-

106 Ibarquengoitia et al., 2006, 2012; Sandri et al., 2014). Recently, Fitzgerald  
107 et al. (2014) proposed a new probabilistic approach based on the model of  
108 Tsunematsu et al. (2014), in which crucial ESPs were quantified in terms of  
109 mean value and standard deviation from the study of 3587 impact craters.

110 We propose a new approach to assess the hazard and the impact on  
111 the built environment related to the ejection of ballistic blocks, compiled in  
112 a package called *Great Balls of Fire* (GBF; Lewis & Hammer, 1957, Sun  
113 Studio). The first part of the GBF package comprises a model written in  
114 Scala, with the main features being i) the stochastic sampling of ESPs, ii) the  
115 implementation of a variable drag coefficient, iii) the ability to use a DEM to  
116 account for topographic barriers and iv) the possibility to work on a single  
117 CPU or on a cluster of computers. The second part of the package provides  
118 *Matlab* routines to post-process model outputs into probabilities of VBP  
119 impacts to exceed energy thresholds, exporting results in a shape readable  
120 by most GIS platforms. This paper first describes the ballistic model, which is  
121 then tested and validated using field measurements of VBPs produced during  
122 the last Vulcanian eruption of La Fossa Volcano, Vulcano Island, Italy. We  
123 then constructed an eruption scenario for a Vulcanian eruptive style and  
124 applied the method to compile probabilistic hazard maps for the ejection of  
125 VBPs at La Fossa. Outcomes are combined with a rapid assessment of the  
126 built environment to produce a first-order pre-event impact assessment of  
127 the buildings stock.

## 128 2. Case study of Vulcano Island

129 Vulcano is the southernmost island of the Aeolian archipelago and, along  
130 with Lipari and Stromboli, one of the active volcanic systems of the archipelago  
131 (De Astis et al., 1997; Gioncada et al., 2003, Fig. 1). The sub-aerial activity  
132 of Vulcano started between 135 and 120 ka (Zanella et al., 2001), after which  
133 volcanism migrated N–NW, generating a composite structure of four, juxta-  
134 posed volcanic edifices including the cone of La Fossa, center of the current  
135 activity. The eruptive history and structure of the 391 m-high La Fossa cone  
136 has been studied by Keller (1980), Frazzetta et al. (1983), Frazzetta et al.  
137 (1984), Gioncada et al. (2003), Arrighi et al. (2006), Dellino et al. (2011), De  
138 Astis et al. (2013) and Di Traglia et al. (2013).

139 The eruptive history of the last 1,000 years was reconstructed based  
140 on stratigraphic studies (Di Traglia, 2011; De Astis et al., 2013) and his-  
141 torical chronicles (Mercalli and Silvestri, 1891; De Fiore, 1922). Following

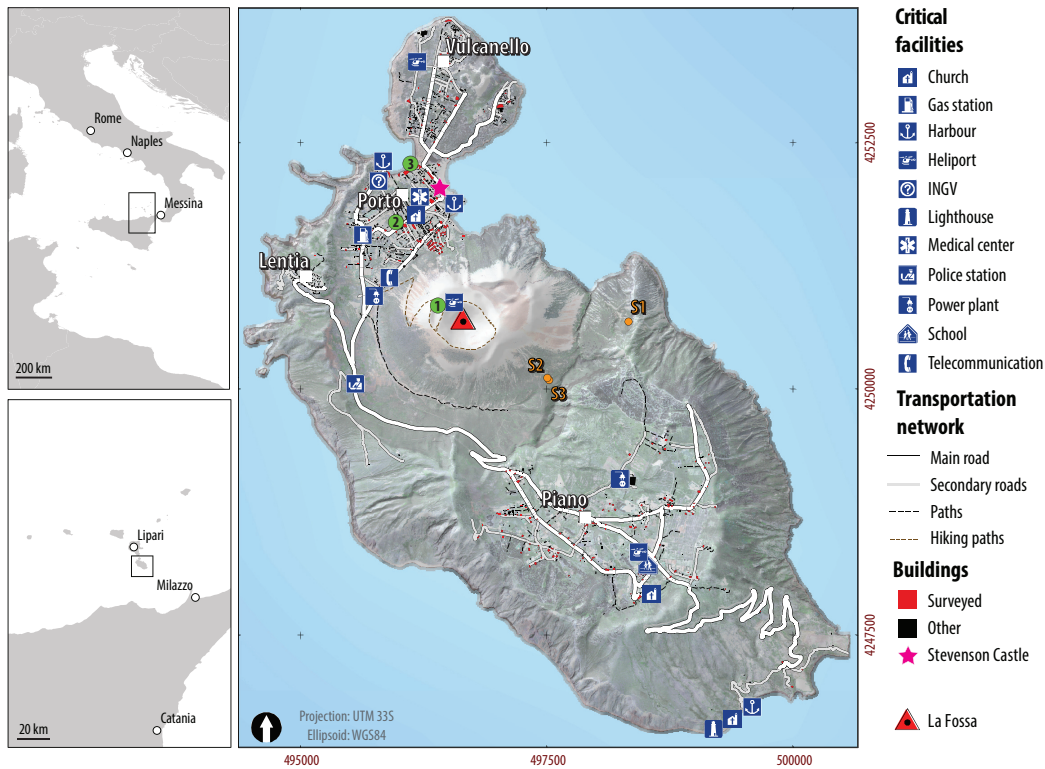


Figure 1: Overview of Vulcano Island, showing the main localities used throughout the text (white squares), the road network, the location of critical infrastructures and buildings footprints. Green dots show the reference points used for the sensitivity analysis. Orange dots show the field location of the sampling sites. Adapted from Biass et al. (2016).

142 the nomenclature of Di Traglia et al. (2013), the most recent deposits were  
 143 grouped in two stratigraphic clusters including the Palizzi–Commenda Erup-  
 144 tive Cluster (PCEC) and the Gran Cratere Eruptive Cluster (GCEC).

145 The PCEC is divided in the Palizzi and the Commenda units (Frazzetta  
 146 et al., 1983, 1984; Dellino and La Volpe, 1997; Di Traglia, 2011; Dellino et al.,  
 147 2011; De Astis et al., 2013). The Palizzi unit is a semi-persistent eruptions  
 148 characterized by shifts between explosive and effusive styles, for which no  
 149 VBP is identified in the stratigraphy. The Commenda unit is a magmatic–  
 150 hydrothermal eruption (Gurioli et al., 2012) that produced the Breccia di  
 151 Commenda deposit (~1240AD), characterized by a high lithic-to-juvenile  
 152 ratio and dense lithic VBPs (Gurioli et al., 2012; Di Traglia et al., 2013).

153 The GCEC (1440AD–1890AD; Di Traglia et al., 2013) started with a

154 steam–blast eruption on the 5<sup>th</sup> of February 1444 (Mercalli and Silvestri,  
 155 1891). Around 1550AD occurred the first of the eight Vulcanian eruptions  
 156 of the GCEC (Di Traglia et al., 2013). The last eruption occurred in 1888–  
 157 1890 and was characterized by plume heights between 1 and 10 km and an  
 158 intense ejection of VBPs. Different morphologies were produced at various  
 159 stages of the eruption, with dense lithic blocks occurring at the beginning and  
 160 the end of the cycle and juvenile breadcrust bombs ejected mostly halfway  
 161 through the eruption (Bianchi, 2007; Di Traglia, 2011). Outcrops with VBPs  
 162 associated with the 1888–1890 eruption are shown in Figure 1 (S1–S3). In  
 163 addition, historical reports also mention that a warehouse located close to  
 164 the so-called Stevenson Castle (pink star on Fig. 1) was impacted by a VBP.

165 About 800 people permanently live on Vulcano, but daily peaks can reach  
 166 20,000 during the summer season. Four settlements are present on the island.  
 167 In the south, Piano lies on top of the filled caldera of Vulcano Primordiale and  
 168 is the home of most of the permanent inhabitants. The remaining settlements  
 169 of the Porto area, Vulcanello and Lentia, comprise most of the hotels and  
 170 tourism facilities. The topography (Fig. 1) suggests that Piano and Lentia  
 171 are sheltered by barriers, whereas the Porto and Vulcanello areas lie on a  
 172 plain directly North of the La Fossa cone.

### 173 3. The GBF Model

174 The GBF model is based on classical movement equations using gravity  
 175 and drag force and accounts for a standard atmosphere, the influence of the  
 176 wind and a region of reduced drag following Mastin (2001). The simulator was  
 177 implemented using the Scala language and parallelized with the Akka actor  
 178 framework. User interactions are provided through a minimalist command  
 179 line interface and all simulation settings are defined in a simple configuration  
 180 file.

#### 181 3.1. Governing equations

182 Each particle is approximated by a sphere and described by a mass  $m$ ,  
 183 an average diameter  $D$ , a position  $\mathbf{r}$  and a velocity  $\mathbf{v}$ . The VBP trajectory  
 184 is described by the following equations:

$$\mathbf{u} = \mathbf{v} - \mathbf{w} \tag{1}$$

$$\ddot{\mathbf{r}} = \dot{\mathbf{v}} = \mathbf{a} = \frac{-\rho_a A C_d \mathbf{u} |\mathbf{u}|}{2m} + \mathbf{g} \tag{2}$$

186 where  $A$  is the fluid cross area,  $C_d$  the drag coefficient,  $\rho_a$  the air density,  
 187  $\mathbf{u}$  the velocity of the VBP relative to the wind  $\mathbf{w}$  and  $\mathbf{g}$  the acceleration  
 188 gravity vector. The computation of the drag coefficient and the air density  
 189 depends on the VBP altitude and velocity. For a given altitude  $z$ , the air  
 190 temperature  $T$  and pressure  $p$  are computed using the following formulas:

$$T(z) = T_0 + \gamma z \quad (3)$$

$$p(z) = p_0 \left( \frac{T(z)}{T_0} \right)^{-\frac{g}{R\gamma}} \quad (4)$$

191 where  $T_0$  and  $p_0$  are respectively the air temperature and pressure at  
 192 sea level,  $\gamma$  is the thermal lapse and  $R$  the gas constant. This allows the  
 193 computation of both the air density and the kinematic viscosity  $\nu_a$ :

$$\rho_a(z) = \frac{p(z)}{RT(z)} \quad (5)$$

$$\nu_a(z) = \left( \frac{6.70810^{-3}}{T(z) + 117} \right) \cdot \left( \frac{T(z)}{273} \right)^{\frac{3}{2}} \quad (6)$$

194 The particle Reynolds number, based on the air characteristics detailed  
 195 above and the VBP diameter and speed, is used to determine the drag coef-  
 196 ficient  $C_d$ :

$$Re = \frac{\rho_a u D}{\nu_a} \quad (7)$$

$$C_d = \begin{cases} 0.1 & \text{if } Re < 3 \times 10^5, \\ 0.5 & \text{else.} \end{cases} \quad (8)$$

197 Since VBPs are ejected together with an expanding mass of gas, the drag  
 198 coefficient may be reduced according to the following equation:

$$C'_d = \begin{cases} C_d \left( \frac{r}{r_d} \right)^2 & \text{if } r < r_d, \\ C_d & \text{else.} \end{cases} \quad (9)$$

Table 1: Summary of parameters modelled stochastically in the GBF model.  $N(\mu, \sigma)$  represents a Gaussian distribution with average  $\mu$  and standard deviation  $\sigma$ .  $U(a, b)$  represents a uniform distribution with values in the interval  $[a, b]$ .

Parameter	Distribution	Constraint
Ejection velocity ( $v$ )	$\in N(v_\mu, v_\sigma)$	$v > 0$
Ejection angle ( $\phi$ )	$\in  N(\phi_\mu, \phi_\sigma) $	
Ejection azimuth ( $\theta$ )	$\in U(0, 2\pi)$	
Density ( $d$ )	$\in N(d_\mu, d_\sigma)$	$d > 0$
Grain size ( $\Phi$ )	$\in N(\Phi_\mu, \Phi_\sigma)$	

199 *3.2. Random VBP generation*

200 The GBF model is implemented with a module for generating VBPs  
 201 with random initial conditions. Each VBP is generated with ESPs sampled  
 202 stochastically and constrained either on Gaussian or uniform distributions  
 203 (Table 1). Each VBP is characterized by a diameter and a density, which,  
 204 assuming a spherical shape, are used to calculate the mass. Additional tests  
 205 are performed to ensure that all constraints in Table 1 are satisfied, else all  
 206 parameters are discarded and re-sampled.

207 *3.3. Numerical model and implementation*

208 Equations 1–9 are solved numerically using Runge-Kutta 4th order with  
 209 a time step  $\Delta t = 0.01$  s. In the absence of an analytic solution, we tested  
 210 the accuracy of the output by solving the trajectories of 10,000 randomly  
 211 sampled VBPs with time steps of 0.01 s and 0.001 s. Using the smaller time  
 212 step as a reference, we computed the absolute error as the distance between  
 213 impact points under both conditions. The error was  $<1$  m for 99.56% of the  
 214 VBPs and the maximum recorded error was  $<3$  m. When normalized by the  
 215 distance between the impact and the vent, only 9 VBPs out of 10,000 had a  
 216 relative error of  $>0.01\%$ .

217 *3.4. Validation with field data*

218 The GBF model was validated using the field observation of six VBPs  
 219 associated with the 1888–1890 eruption presenting sufficient stratigraphic  
 220 constraints to discard possible reworking and displacement. The VBPs were  
 221 classified in three typical morphologies including i) lithic blocks, either fresh  
 222 or altered, ii) thin-rinded breadcrust bombs and iii) thick-rinded breadcrust  
 223 bombs.



224 Firstly, the S1 sampling site (Fig. 1; Table 2) comprises one thick-rinded  
 225 breadcrust bomb identified by Bianchi (2007) characterized by a diameter of  
 226 25 cm and a density of  $1800 \text{ kg m}^{-3}$ , located  $\sim 1560 \text{ m}$  from the vent. Using  
 227 the *Eject!*, Bianchi (2007) identified two extreme solutions to reproduce this  
 228 field observation. On one end, a minimum ejection velocity of  $145 \text{ m}\cdot\text{s}^{-1}$  was  
 229 identified using an ejection angle of  $45^\circ$  from vertical. Based on the obser-  
 230 vations of steep crater slopes during the 1888–1890 eruption (Mercalli and  
 231 Silvestri, 1891), an inclination of  $15^\circ$  from the vertical was used to represent  
 232 a more realistic ejection angle. Such an angle results in an ejection velocity of  
 233  $350 \text{ m}\cdot\text{s}^{-1}$ , which is comprised in the higher spectrum of velocities reported in  
 234 the literature for Vulcanian explosions (e.g. Druitt et al., 2002; Wright et al.,  
 235 2007; Alatorre-Ibargüengoitia et al., 2012; Maeno et al., 2013). Secondly,  
 236 the S2 sampling site represents a  $20 \times 20 \text{ m}$  area where the populations of  
 237 different VBPs morphologies were studied. From a total of 111 VBPs found  
 238 in the area, the S2 sampling site shows a dominance of lithic blocks (80%)  
 239 with minor thin- (14%) and thick-rinded (6%) breadcrust bombs. At the  
 240 time of the sampling (performed before and for a different purpose than the  
 241 present paper), the diameter of the most representative VBP of the dominant  
 242 size population of each morphology was estimated (Table 2). Finally, the S3  
 243 sampling site consists of one abnormally large thick-rinded breadcrust bomb  
 244 (Table 2).

245 We used the GBF model to estimate the ejection velocity and angle re-  
 246 producing these observations. Sets of simulations of  $10^5$  particles were per-  
 247 formed, varying the ejection velocities between  $100\text{--}350 \text{ m}\cdot\text{s}^{-1}$  with increment  
 248 of  $25 \text{ m}\cdot\text{s}^{-1}$ , and angles between  $5\text{--}45^\circ$  from the vertical every  $5^\circ$ . At each  
 249 increment, both ejection velocities and angles were allowed a variation char-  
 250 acterized by a standard deviation equal to half of the increment. The mean  
 251 distance calculated over the  $10^5$  VBPs was calculated for each combination  
 252 of ejection velocity and angle.

253 Figure 2 contours the difference between the mean modeled distance and  
 254 the observed distance as a function of ejection velocity and ejection angle.  
 255 The  $0 \text{ m}$  line represents the combination of angle and velocity reproducing  
 256 best the observation, and suggests a continuum of possible solutions. For  
 257 instance, the altered block in the S2 sampling site can equally be reproduced  
 258 by sets of angle and velocities of  $20^\circ/120 \text{ m}\cdot\text{s}^{-1}$  or  $10^\circ/170 \text{ m}\cdot\text{s}^{-1}$  (turquoise  
 259 line in Fig. 2). Radii of reduced drag of 200, 600 and 1,000 m are tested  
 260 (respectively the black, blue and red line in Fig. 2). In general, set of input  
 261 parameters falling the purple region of Figure 2 suggests an overestimation

Table 2: Summary of observed VBPs associated with the 1888–1890 eruption used for the field validation of the GBF model. The distance represents the euclidean distance from the actual vent. The sample locations are reported on Fig. 1. *BCB* stands for breadcrust bomb.

Sampling site	Type	Distance (m)	Axes lengths (cm)	Diameter (cm)	Density ( $\text{kg m}^{-3}$ )	
					Mean	$\sigma$
S1	Thick-rinded BCB	1560	—	25	1600	200
S2	Altered block	960	$120 \times 65 \times 40$	$68^a$	2300	100
S2	Fresh block	960	$40 \times 35 \times 22$	$31^a$	2300	100
S2	Thin-rinded BCB	960	$47 \times 30 \times 10$	$24^a$	800	50
S2	Thick-rinded BCB	960	$35 \times 30 \times 18$	$27^a$	1600	200
S3	Thick-rinded BCB	1000	$70 \times 50 \times 50$	$56^a$	1600	200

<sup>a</sup>: Equivalent diameter expressed as the geometric mean of the three orthogonal axes.

262 compared to field observations, whereas the orange region suggests an un-  
 263 derestimation.

264 For the S1 sample, both the GBF and *Eject!* models result in similar  
 265 minimum conditions, i.e. a velocity of  $145 \text{ m}\cdot\text{s}^{-1}$  for an ejection angle of  $45^\circ$   
 266 (Fig. 2). In contrast, the GBF model suggests a velocity of  $\sim 225 \text{ m}\cdot\text{s}^{-1}$  for  
 267 an angle of  $15^\circ$ , which is significantly lower than the  $350 \text{ m}\cdot\text{s}^{-1}$  suggested  
 268 by Bianchi (2007) but more realistic when compared to typical ejection ve-  
 269 locities reported for Vulcanian explosions (e.g. Druitt et al., 2002; Alatorre-  
 270 Ibarguengoitia et al., 2006; Wright et al., 2007; Alatorre-Ibarguengoitia et al.,  
 271 2012; Maeno et al., 2013). Nevertheless, due to the location of the S1 sample  
 272 (i.e. on the edge of the Piano caldera,  $1.6 \text{ km}$  away from the vent) and the  
 273 absence of historical report of VBP reaching the Piano caldera, we assume  
 274 the S1 sample as an extreme case-figure. The S2 and S3 sampling sites are  
 275 well reproduced by the GBF model (Fig. 2), where an ejection velocity of  
 276  $150 \text{ m}\cdot\text{s}^{-1}$  typically requires ejection angles lower than  $15\text{--}20^\circ$ .

277 Two additional observations can be made from Figure 2. Firstly, the  
 278 S2 sampling site shows that for a similar equivalent diameter, thin-rinded  
 279 breadcrust bombs require higher ejection velocities than thick-rinded bread-  
 280 crust bombs to reproduce the observations, which is due to the lower kinetic  
 281 energy of lighter VBPs. Secondly, an increased radius of reduced drag has an  
 282 overall low influence on the modeled distance, although the effect increases  
 283 when reproducing impacts farther from the vent (e.g. S1) or for lighter VBPs  
 284 (thin-rinded breadcrust bomb of S2).

## 285 4. Application to La Fossa volcano

### 286 4.1. Eruptive scenarios

287 During the activity of the last 1,000 years at La Fossa, two main erup-  
288 tive styles produced VBPs, namely non-juvenile steam blast eruptions (i.e.  
289 Commenda unit) and Vulcanian eruptions (Di Traglia et al., 2013; De Astis  
290 et al., 2013). Here, we only consider a Vulcanian-type scenario because i)  
291 field evidences suggest that the majority of VBPs associated with the Com-  
292 menda unit are displaced, making any validation attempt impossible and  
293 ii) the caprock assumption used for the probabilistic sampling of eruption  
294 scenarios is valid only for Vulcanian eruptions.

295 We developed a Vulcanian-type scenario around the reference 1888–1890  
296 eruption. ESPs were constrained based on data presented in Section 3.4  
297 and the works of Bianchi (2007) and Tsunematsu (2012). Previous authors  
298 have estimated proportions of dense juvenile blocks, thin-rinded and thick-  
299 rinded breadcrust bombs to be respectively 70–90%, 5–15% and 10–20% of  
300 the total observed VBPs. Since proportions of each VBP type obtained at  
301 the sampling site S2 (Fig. 1; Sect. 3.4) fall within these ranges (Mercalli and  
302 Silvestri, 1891; Bianchi, 2007; Di Traglia, 2011), we assume a proportion of  
303 80% of lithic blocks, 14% of thin-rinded and 6% of thick-rinded breadcrust  
304 bombs.

305 Probabilistic hazard assessments rely on the simulation of a large number  
306 of event, stochastically varying ESPs in order to account for the variability  
307 of eruptive processes when predicting future eruptions. Table 3 summarizes  
308 the ESPs for the Vulcanian eruption scenario at La Fossa. Variable param-  
309 eters include i) density ( $\text{kg}\cdot\text{m}^{-3}$ ), ii) VBP diameter ( $\phi$ ), iii) ejection velocity  
310 ( $\text{m}\cdot\text{s}^{-1}$ ) and iv) ejection angle (i.e. azimuth,  $^\circ$  from vertical). The number of  
311 observations being too limited to estimate complex probability distributions  
312 (e.g. based on Tsunematsu, 2012,  $n = 12$  for density measurements and  
313  $n = 40$  for diameter measurements), we used Gaussian distributions centred  
314 on the mean value ( $\mu$ ) and expressing the uncertainty using the standard  
315 deviation ( $\sigma$ ), which accounts for about 68.3% of the population.

316 The density associated with various types of VBPs was discretized in  
317 three different ranges. Separate runs were performed for each VBP type by  
318 i) adjusting the density range and ii) scaling the number simulated parti-  
319 cles to reproduce the proportions of each VBP type. The mean densities  
320 and associated standard deviations of blocks, thin-rinded and thick-rinded  
321 breadcrust bombs were set to  $2300 \pm 100$ ,  $800 \pm 50$  and  $1600 \pm 200 \text{ kg}\cdot\text{m}^{-3}$ ,

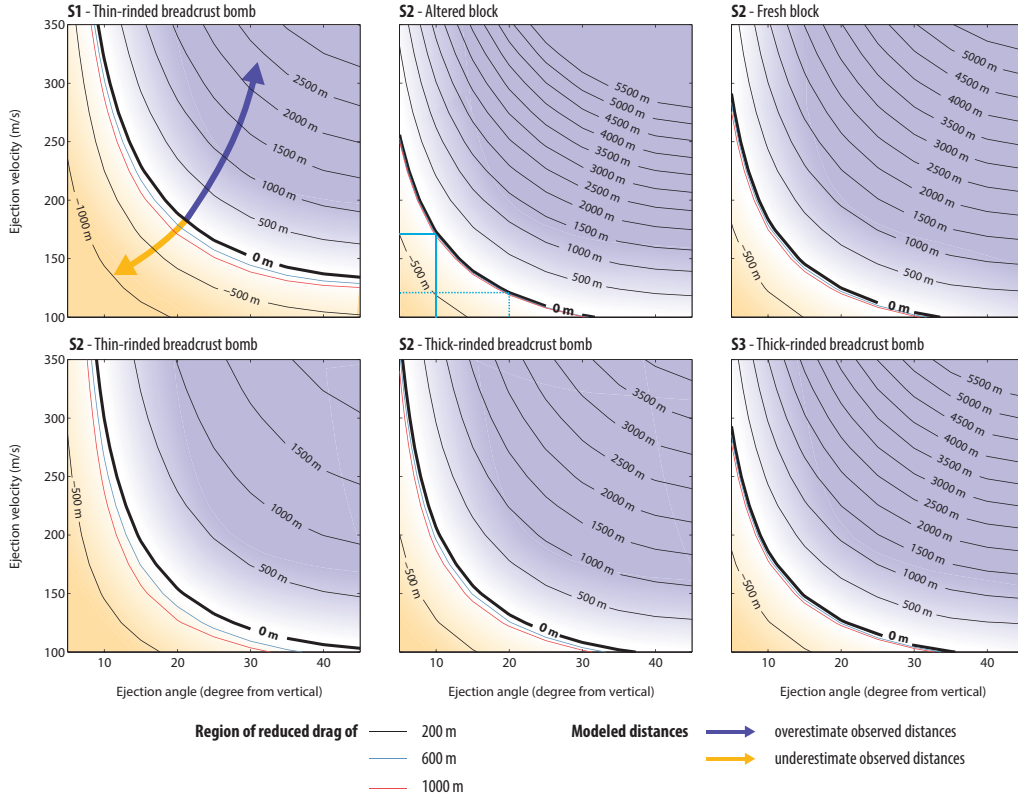


Figure 2: Difference (in metres) between the mean modeled distance and the observed distance as a function of ejection velocity and ejection angle for all VBP morphologies observed at sampling sites shown in Fig. 1 (orange dots). The white region represents sets of input parameters reproducing best observations. Radii of 200 m (black lines), 600 m (blue line) and 1,000 m (red line) are considered.

322 respectively. The diameter is expressed on a Gaussian distribution in  $\phi$  units,  
 323 which results in a log-normal distribution when converted to metres. The  
 324 mean diameter considered is  $-7.65\phi$  (i.e. 0.2 m) with a  $\sigma_{Diam} = 1.2\phi$ . In  
 325 meters, the  $\mu - \sigma$  and  $\mu + \sigma$  are 0.09 and 0.46 m, respectively. The median  
 326 ejection velocity was set to  $100 \text{ m}\cdot\text{s}^{-1}$  with a  $\sigma_{Vel} = 50 \text{ m}\cdot\text{s}^{-1}$ , which scales  
 327 with published values for Vulcanian eruptions (Druitt et al., 2002; Alatorre-  
 328 Iburgüengoitia et al., 2006; Wright et al., 2007; Alatorre-Iburgüengoitia et al.,  
 329 2012; Maeno et al., 2013). The ejection angle was defined as a mean value  
 330 centred on the vertical with a standard deviation of  $\frac{\pi}{12}$  rad, i.e.  $15^\circ$ .

331 A standard atmosphere, no wind and a radius of reduced drag of 200 m

Table 3: Eruption source parameters associated with a Vulcanian-type eruption scenario at La Fossa volcano based on the 1888–1890 eruption. Different Gaussian distributions of densities are identified for <sup>a</sup> lithic blocks, <sup>b</sup> thin-rinded and <sup>c</sup> thick-rinded breadcrust bombs.

		Unit	Mean	$\sigma$
<b>Source</b>	Density		2500	100 <sup>a</sup>
			800	50 <sup>b</sup>
			1600	200 <sup>c</sup>
	Diameter	$\phi$	-7.65	1.2
	Velocity	m·s <sup>-1</sup>	100	50
	Ejection angle	rad	0	$\pi / 12$
	Number particles	—	10 <sup>6</sup>	—
<b>Wind</b>	Speed	m·s <sup>-1</sup>	0	—
	Direction	Degree	0	—
<b>Drag</b>	Time step	s	0.01	—
	Pressure	hPa	$1.01325 \times 10^5$	—
	Temperature at sea level	° K	298	—
	Thermal lapse	° C km <sup>-1</sup>	$-6.5 \times 10^{-3}$	—
	Reduced Drag radius	m	200	—

332 were used to calculate drag forces (Mastin, 2001). Alatorre-Ibargüengoitia  
333 et al. (2012) report heights of about 600 m at Popocatepetl volcano, which  
334 we chose to reduce since these explosions appear larger and characterized  
335 by higher ejection velocities and distances reached by VBPs. Additionally,  
336 as discussed in Section 3.4, the radius drag is of limited importance in such  
337 proximal distances to the vent (Fig. 2). It is however important to notice  
338 that in the case of La Fossa, an altitude of 200 m above the vent is higher  
339 than the surrounding crater.

#### 340 4.2. Probabilistic hazard assessment

341 The destructiveness caused by VBPs is mostly due to the high kinetic en-  
342 ergy at impact; the aim of this hazard assessment is thus to investigate the  
343 probability to exceed critical energy thresholds. Various thresholds, hereafter  
344 expressed as  $E_T$  (J), were identified as potential threats to the built environ-  
345 ment (e.g. Pomonis et al., 1999; Spence et al., 2005; Jenkins et al., 2014) and  
346 will be discussed later. Since VBPs result in discontinuous punctual impacts,  
347 it is necessary to average the number of impacts on a representative area.  
348 Since no standardized method yet exists, we explore two different approaches  
349 to quantify the hazard related to VBPs impacts.

350 *4.2.1. Pixel-based approach*

351 First, we average the VBP impacts on an equally-spaced grid. The prob-  
 352 ability of occurrence a VBP of a given energy threshold in a pixel  $i, j$  of area  
 353  $A$  is quantified as:

$$P(A_{i,j}, E_T) = \frac{\sum VBP_{A_{i,j}, E_T}}{n_{VBP}}, \quad (10)$$

354 where  $n_{VBP}$  is the total number of simulated VBPs.

355 Since this approach introduces a dependency to the pixel area, we assess  
 356 the sensitivity of our post-processing method to i) the number of VBPs  
 357 simulated and ii) the resolution of the grid used to compile probabilistic  
 358 hazard assessments. The number of simulated VBPs was varied between  $10^4$   
 359 and  $10^7$  with increment of  $10^1$ . Grid resolutions of 5, 10, 20, 50, 75, 100, 200,  
 360 300, 400, 500, 600, 700, 800, 900 and 1,000 m were tested. 20 simulations  
 361 were performed for each combination of number of particles/grid resolution.  
 362 The probability to exceed an impact energy of 4,000 J was computed for the  
 363 top of the hiking path, the center of the Porto area and Porto di Ponente  
 364 (green points 1, 2, and 3 on Fig. 1, located 400, 1,300 and 1,700 m from  
 365 the vent, respectively). This threshold represents the minimum energy to  
 366 penetrate weak RC slabs roofs (Spence et al., 2005).

367 Figure 3 summarizes the sensitivity analysis. For a given combination of  
 368 number of particles/grid resolution, we assess the sensitivity based on the  
 369 mean probability  $P(A_{i,j}, 4000J)$  (i.e. left y axis) and the associated standard  
 370 deviation (right y axis) calculated over the 20 simulations. The x axis repre-  
 371 sents the resolution of the equally spaced grid, where the pixel area  $A$  is the  
 372 square of the grid spacing. Each column of plots contains results for a dif-  
 373 ferent location, with distance from the vent increasing from left to right (Fig  
 374 1). Each row represents an increase of the number of simulated particles.  
 375 Results show that:

- 376 • For a given point, an increase of the number of simulated particles does  
 377 not significantly affect the mean probability value but greatly reduces  
 378 the associated standard deviation;
- 379 • For a given number of simulated particles, the probability decreases  
 380 with distance from the vent but the standard deviation remains in the  
 381 same order of magnitude;
- 382 • For the proximal point (i.e. Point 1 in Fig. 3), a change of order of  
 383 magnitude of mean probabilities (i.e.  $10^{-2}\%$  to  $10^{-1}\%$ ) occurs at a

384 resolution of about 200 m.

385 Based on these observations, we simulate  $10^6$  particles averaged on a  $100 \times$   
386 100 m grid, which provides a compromise between computation time and  
387 accuracy of the output. In the absence of a plateau with stable probability  
388 values, we fix the resolution threshold in the zone of the lowest variability of  
389 mean probability values.

#### 390 *4.2.2. Zone-based approach*

391 Second, we assess the probability of impact in a zone of interest  $Z$ . Here,  
392 such a zone is defined either as a distance from the vent (i.e. the probability  
393 of impact at a given distance interval from the vent) or as a radial sector (i.e.  
394 probability of impact at a given azimuth interval from the vent). Probabilities  
395 of a VBP exceeding an energy threshold  $E_T$  can then be normalized either on  
396 the total number of VBPs simulated or on the number of VBPs that fell in  
397 a given zone  $Z$ . In the first case,  $P(Z, E_T)$  answers the question "what is the  
398 probability of a VPB to exceed a given energy threshold  $E_T$  in a zone  $Z$ ".  
399 In the second case,  $P(E_T|Z)$  answers the question "knowing that a VBP  
400 impacts the zone  $Z$ , what is its probability to exceed an energy threshold  
401  $E_T$ ".

402 Note that although the combination of both approaches might result in  
403 an overall picture of the VBP hazard around a given volcano, the comparison  
404 of the hazard with other volcanoes is difficult due to the nature of both the  
405 modelling and the post-processing methods. Additionally, each approach to  
406 the probabilistic quantification of the VBP hazard have different purposes.  
407 For instance, the zone-based approach is more suitable for hazard zoning  
408 purposes, whereas the pixel-based approach is more appropriate for impact  
409 assessment purposes. For this reason, this latter one will be discussed in more  
410 details in this paper, but the zone-based approach is thoroughly presented  
411 in the user-manual of the GBF model.

#### 412 *4.3. Vulnerability of the built environment*

413 The high kinetic energy of VBPs can result in damages to the structures,  
414 roof perforation or collapse of the building (Blong, 1984; Pomonis et al.,  
415 1999; Spence et al., 2005; Jenkins et al., 2014). The likelihood of a building  
416 to suffer damages is typically expressed by vulnerability curves describing the  
417 relationship between the intensity of the hazard and the probability of dam-  
418 age. Such a relationship is commonly defined through a combination of i)

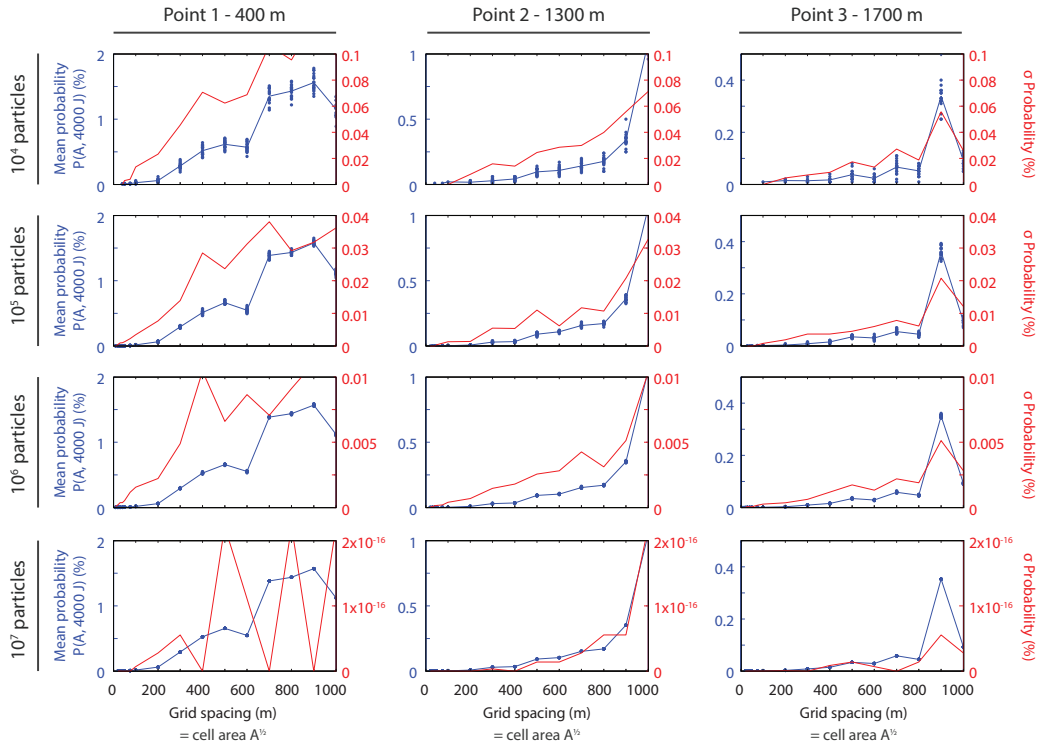


Figure 3: Sensitivity of the probabilistic hazard assessment strategy to i) the number of simulated particles and ii) the resolution of the grid used to quantify the probability of VBPs exceeding a given energy threshold  $E_T$  of 4,000 J. Across sub-plots, the rows represent variable number of simulated particles and the columns represent the different points on which probabilities were calculated (i.e. green points in Fig. 1) and include the top of the hiking path (Point 1; 400 m from the vent), the center of the Porto area (Point 2; 1,300 m from the vent) and Porto di Ponente (Point 3; 1,700 m from the vent). Each plot has two y-axes: the left one (blue) shows the mean probability calculated over the 20 simulations (blue dots) for each set of number of particles/grid resolution; the right one (red) shows the corresponding standard deviation.

419 post-event damages studies (e.g. Pomonis et al., 1999; Blong, 2003b; Wilson  
 420 et al., 2011), ii) laboratory experiments and iii) theoretical studies on mate-  
 421 rial strengths (e.g. Petrazzuoli and Zuccaro, 2004). Volcanic eruptions being  
 422 multi-hazards systems, each hazard requires different vulnerability function.  
 423 In the case of tephra fallout, such a function describes the relationship be-  
 424 tween tephra load and impact. For VBPs, the parameter of importance is  
 425 the kinetic energy at the impact.

426 Here, we assess the vulnerability of buildings to roof perforation from



427 VBP impacts. The starting point of this study is the vulnerability curves  
 428 proposed by Spence et al. (2005) for the tephra hazard in Europe. Vulner-  
 429 ability curves take the shape of a cumulative density function of a Normal  
 430 distribution ( $\phi$ ) and are expressed as a function of the mean kinetic energy  
 431  $E_{mean}$  and  $\sigma$ . Following Spence et al. (2005) and Jenkins et al. (2014), the  
 432 probability of perforation ( $P_{perforation}$ ) is expressed as a function of the VBP  
 433 energy  $I$  (J) with the following relationship:

$$P(Perforation|I) = \phi(\ln(I), \ln(E_{mean}), \sigma) \quad (11)$$

434 Two aspects require care when Equation 11 is used. Firstly, although  $\phi$   
 435 represents the standard form of a cumulative density function of a Normal  
 436 distribution, both  $I$  and  $E_{mean}$  are expressed in natural logs, which results  
 437 in a log-normal distribution (Spence et al., 2005). Secondly, although  $\sigma$  is  
 438 often referred to as *standard deviation*, which suggests that it has the same  
 439 unit as the mean, it is in fact a coefficient of variation expressed between 0  
 440 and 1. Therefore, when Spence et al. (2005) suggests that “ $\sigma$  is 20% of the  
 441 mean”, it implies the use of a coefficient of variation of 0.2.

442 Biass et al. (2016) provide a review of the built environment in Vulcano.  
 443 The 2000 census of the Italian Istituto Nazionale di Statistica (ISTAT, 2005)  
 444 identifies 1093 buildings on the island, comprising 895 residential houses and  
 445 64 public and tourism facilities. According to this census, the main construc-  
 446 tion period spans from the 1970’s to 1980’s, but discussions with inhabitants  
 447 and workers on the island suggest that most buildings were renovated over  
 448 the years, making the true period of construction difficult to assess. Addi-  
 449 tionally, the field survey performed in the context of the EU-funded *ENSURE*  
 450 project (Bonadonna et al., 2011) provides detailed descriptions of the most  
 451 representative building in a  $100 \times 100$  m pixel, revealing that building mor-  
 452 phologies are homogeneously distributed over the settled areas and include  
 453 70% single-storey buildings, 73% with flat roofs and 54% with a regular mor-  
 454 phology. Additionally, building’s footprints were mapped from aerial images  
 455 (Bonadonna et al., 2011).

456 Here, we adapted the method of Spence et al. (2005) for the specific  
 457 case of Vulcano and for the VBP impact. Firstly, following Biass et al.  
 458 (2016), we assume that buildings either have flat reinforced concrete roofs  
 459 or tiled roofs over a timber structure in good or average conditions. These  
 460 observations were compared with those of Spence et al. (2005) to define the  
 461 roof classes in Table 4. Secondly, vulnerability curves of Spence et al. (2005)

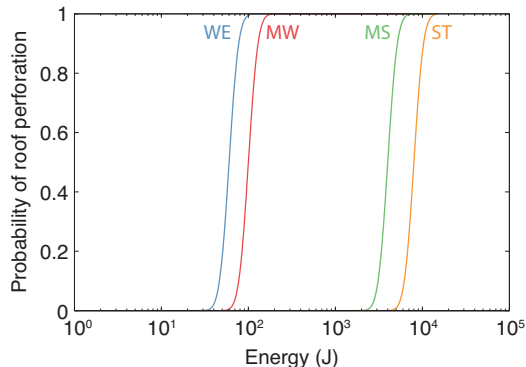


Figure 4: Vulnerability curves for the roof types *WE*, *MW*, *MS* and *ST* of Spence et al. (2005) as defined in Table 4.

Table 4: Description of the typical roofing stocks of Spence et al. (2005) adapted to the built environment of Vulcano (adjusted from Biass et al. (2016)). The vulnerability of each roof class is characterized by a mean kinetic energy  $E_{mean}$  and a standard deviation  $\sigma$  fixed to 0.2. The  $E_{mean}$  is identified based on existing literature Spence et al. (2005); Tsunematsu (2012); Pomonis et al. (1999); Jenkins et al. (2014); Blong (1984); Mavrouli and Corominas (2010b). *RC* stands for reinforced concrete.

Roof class	Description	$E_{mean}$ (J)
<b>WE (weak)</b>	Tiled roof, poor condition	60
<b>MW (medium weak)</b>	Tiled roof, average or good condition	100
<b>MS (medium strong)</b>	Flat RC roof , average condition	4,000
<b>ST (strong)</b>	Flat RC roof, good condition	8,000

462 were adapted to express the probability of roof perforation as a function  
 463 of the kinetic energy at impact. We estimated the mean energies  $E_{mean}$  of  
 464 each roof class (Equation 11) based on published literature (e.g. Spence  
 465 et al., 2005; Tsunematsu, 2012; Pomonis et al., 1999; Jenkins et al., 2014;  
 466 Blong, 1984). Following the approach applied to tephra fallout, the standard  
 467 deviation of the distribution ( $\sigma$ ) was fixed to 0.2 (Spence et al., 2005; Jenkins  
 468 et al., 2014). Figure 4 illustrates the vulnerability curves for the roof classes  
 469 defined in Table 4.

## 470 5. Results

471 For the scenario identified in Table 3, Figure 5A shows the variation  
 472 of the median VBP energy with distance from the vent, with the associated

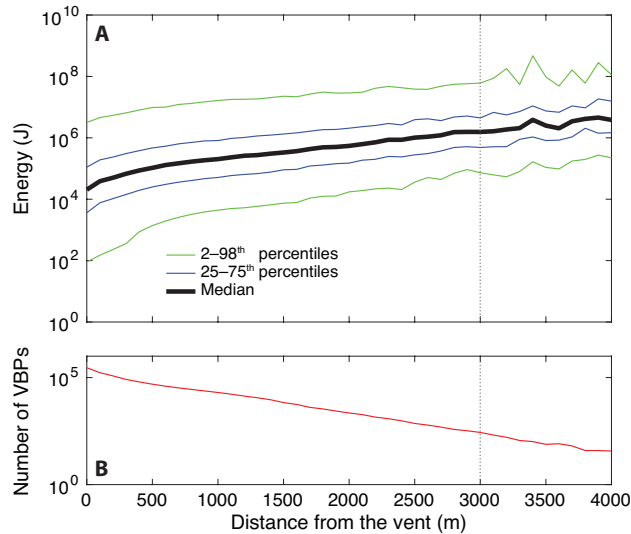


Figure 5: A: Median energy with distance from the vent. The uncertainty is expressed by the 25<sup>th</sup>–75<sup>th</sup> and the 2<sup>nd</sup>–98<sup>th</sup> percentiles. The vertical dashed line indicates the distance (i.e.  $\sim 3,000$  m) at which the number of particles is too limited to produce stable results. B: Number of particles with distance from the vent, suggesting that only  $\sim 10^3$  VBPs fall beyond a distance of  $\sim 3,000$  m.

473 variability expressed as the 25<sup>th</sup>–75<sup>th</sup> percentiles and the 2<sup>nd</sup>–98<sup>th</sup> percentiles.  
 474 Two main observations must be outlined from Figure 5A. Firstly, the median  
 475 energy increases with distance from the vent, which is a consequence of the  
 476 caprock assumption used to model Vulcanian explosions (Self et al., 1979;  
 477 Wilson, 1980; Fagents and Wilson, 1993). Such an assumption implies that  
 478 once the coherent plug reaches its fragmentation level (here considered as the  
 479 reduced drag radius in Table 3), all VBPs are released with the same ejection  
 480 velocity, regardless of their masses. As a result, only large VBPs possess a  
 481 sufficient kinetic energy to reach distances further away from the vent and  
 482 are therefore associated with relative high impact energies. Secondly, curves  
 483 in Figure 5A follow a smooth trend up to a distance of  $\sim 3,000$  m (i.e.  
 484 vertical dashed line in Fig. 5), after which they become chaotic. Projecting  
 485 this distance on Figure 5B suggests that only  $10^3$  particles are falling at  
 486 distances larger than  $\sim 3,000$  m (i.e. 0.1% of the total number of simulated  
 487 VBPs), which is too limited to obtain stable results. Probabilities calculated  
 488 for distances from the vent larger than  $\sim 3,000$  m should thus be critically  
 489 used.

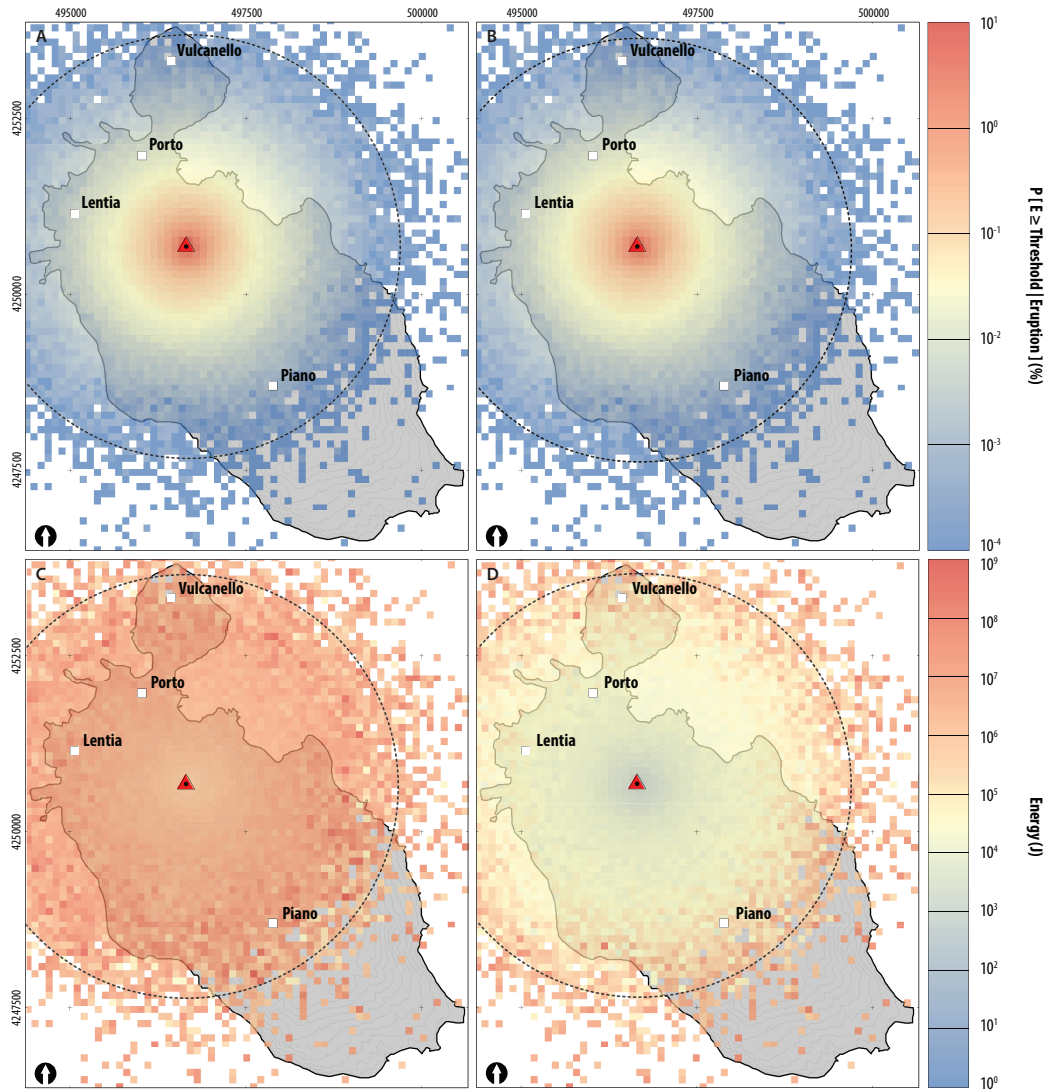


Figure 6: A–B: Probability maps (%) of VBPs exceeding energies of (A) 60 J and (B) 8,000 J. C–D: Energy maps for probabilities of occurrence within a given pixel of (C) 10% and (D) 90%. The main towns are shown as white squares. The black dashed line contours a distance of 3,000 m around the vent, considered as the distance beyond which not enough particles are observed to provide stable results (Fig. 5). Probabilities are conditional to the occurrence of the eruption scenario.

491 We start by quantifying the probability of a VBP impact to exceed energy

492 thresholds hazardous for roof perforation. Note that probabilities expressed  
 493 here are based upon the conditional probability of occurrence of the asso-  
 494 ciated eruption scenario. Following the pixel-based approach, Figure 6A–B  
 495 shows the geographical distribution of probabilities to exceed kinetic energies  
 496 of 60 J (i.e. threshold for the perforation of tiled roofs in poor condition) and  
 497 8,000 J (i.e. threshold for the perforation of reinforce concrete roofs in good  
 498 condition). Impacts are averaged on a  $100 \times 100$  m pixel and normalized over  
 499 the total number of simulated VBPs. Following the zone-based approach,  
 500 we estimate probabilities of impact at a given distance from the vent (Fig.  
 501 7A–B) or at a given radial sector around the vent (Fig. 7C–D). Probabilities  
 502 are expressed either as normalized over the total number of simulated VBPs  
 503 (i.e.  $P(Z, E_T)$ ; Fig. 7A,C) or as normalized over the number of VBPs that  
 504 impacted the considered zone (i.e.  $P(E_T|Z)$ ; Fig. 7B,D). Finally, hazard  
 505 curves were compiled (Fig. 8), which show the probability of exceeding any  
 506 impact energy for the settled areas of Porto, Il Piano, Lentia and Vulcanello  
 507 (white squares in Fig. 1 and Fig. 6), located respectively 1.3, 2.4, 1.8 and  
 508 2.6 km away from the vent.

509 Figure 6A–B suggests little difference in the final probability values for  
 510 the energy thresholds considered for the built environment on Vulcano. This  
 511 observation is confirmed by Figure 8, which shows almost constant proba-  
 512 bility values up to critical energy thresholds of  $10^4$  J for Porto and Lentia  
 513 and  $10^5$  J for Vulcanello and Piano. As a result, probabilities presented  
 514 throughout this section are equal for all energy thresholds relevant for the  
 515 built environment of Vulcano. Porto (1.3 km N of the vent) and Lentia (1.8  
 516 km NW of the vent; Fig 1) are the most exposed settlements with probabili-  
 517 ties of  $\sim 10^{-2}\%$  and  $\sim 5 \times 10^{-3}\%$ , respectively. The settlements of Il Piano  
 518 and Vulcanello, located at respectively 2.4 km SW and 2.6 km N of the vent  
 519 (Fig 1) result in probabilities of  $7 \times 10^{-4}\%$  and  $4 \times 10^{-4}\%$ .

520 Using the zone-based approach to assess the probability of impact at a  
 521 given distance from the vent (Fig. 7A–B), the choice of the type of probability  
 522 (i.e.  $P(Z, E_T)$  vs  $P(E_T|Z)$ ) greatly influences the message carried by the  
 523 probabilistic hazard assessment. When normalized over the total number of  
 524 simulated VBPs, Figure 7A shows greater probabilities of being impacted by  
 525 a VPB with a kinetic energy of 4,000 J in proximal area, where a probability  
 526 of  $\geq 10\%$  exists up to a distance of 1 km away from the vent. In contrast,  
 527 Figure 7B shows that should a VBP impact a given distance interval, there  
 528 is a larger probability that it will exceed a kinetic energy of 4,000 J at larger  
 529 distances from the vent. As a result, there is a  $\sim 100\%$  probability that

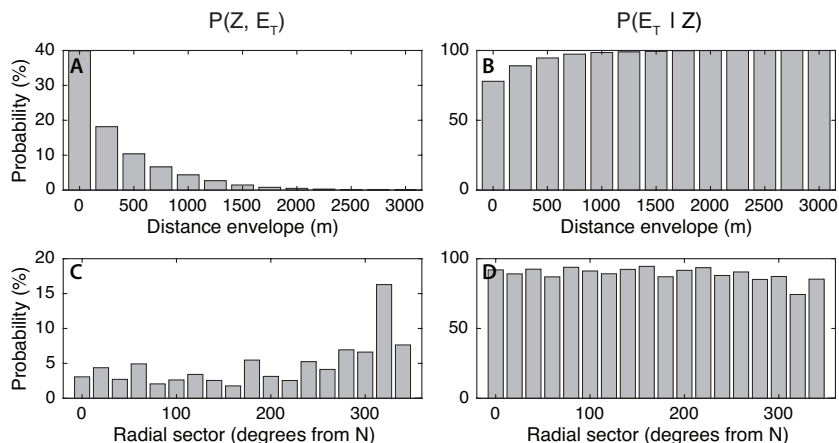


Figure 7: Probabilities of VBPs to exceed a kinetic energy of 4,000 J at a given distance from the vent (A–B) and a given radial sector around the vent (C–D). The left column expresses the probability normalized over the total number of simulated VBPs (i.e.  $P(Z, E_T)$ ) whereas the right column is averaged over the number of VBPs that impacted the considered zone (i.e.  $P(E_T|Z)$ ). Bin sizes are 250 m for the distance and  $20^\circ$  for the radial sectors.

530 a VBP will exceed 4,000 J from a distance of 1 km from the vent. When  
 531 a similar approach is applied on zones of interest defined as radial sectors  
 532 around the vent, Figure 7C shows slightly higher probabilities of the NNW  
 533 sector to be impacted by VBPs ( $P(Z, E_T)$  of 5–15%), which corresponds  
 534 to the lowest part of the crater rim. Figure 7D shows that should a VBP  
 535 impact any radial sector, there is a  $\geq 90\%$  probability that it will exceed an  
 536 energy of 4,000 J.

537 Probabilistic energy maps (Fig. 6C–D) quantify the energy occurring  
 538 at a given probability threshold. At each pixel, the 10<sup>th</sup>, 25<sup>th</sup>, 50<sup>th</sup>, 75<sup>th</sup>  
 539 and 90<sup>th</sup> percentiles were calculated over the energy of all VBPs that fell  
 540 in a given  $100 \times 100$  m area. Since the  $n^{\text{th}}$  percentile returns the lowest  
 541  $n\%$  of the population, there is a  $100 - n\%$  probability that the energy will  
 542 exceed the energy given by the  $n^{\text{th}}$  percentile. As an illustration, the 10<sup>th</sup>  
 543 percentile of a given pixel shows the energy occurring with a 90% probability  
 544 within this given pixel. Note that this energy is based upon the conditional  
 545 probability that a VBP impact is occurring inside this pixel, and does not  
 546 consider the probability of the pixel to be impacted. Figure 6C–D illustrates  
 547 the geographical distributions of energies for probabilities of occurrence of  
 548 10% and 90%, which result in typical kinetic energies of  $10^6$ – $10^7$  and  $10^4$ – $10^5$

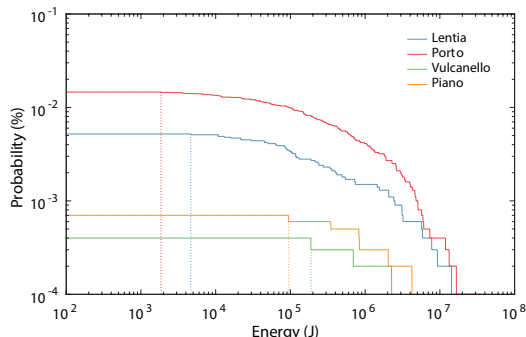


Figure 8: Hazard curves for the urban settlements areas of Porto, Il Piano, Lentia and Vulcanello located 1.3, 2.4, 1.8 and 2.6 km away from the vent, respectively (white squares in Fig. 1 and Fig. 6). Vertical dashed lines show, for each location, the energy threshold below which impacts of any energy have equal probabilities of occurrence.

549 J over Porto, respectively.

## 550 5.2. Pre-event impact assessment

551 The impact was assessed by combining the vulnerability analysis (Table  
 552 4 and Fig. 4) with the probabilistic energy maps (Fig. 6C–D). For each  
 553 building, the energy occurring in the containing pixel is retrieved and used  
 554 in Equation 11 to calculate the probability of roof perforation. Two observa-  
 555 tions can be made here. Firstly, Figure 7A–B suggests similar probabilities to  
 556 exceed VBP impacts of 60 J or 8,000 J. This observation is supported by Fig-  
 557 ure 8, that reveals identical probabilities of occurrence of impacts  $< \sim 3 \times 10^3$   
 558 J for the localities of Lentia and Porto and  $< \sim \times 10^5$  J for the Vulcanello  
 559 and Piano. Secondly, Figure 7C–D indicates that energies of  $\sim 10^4$  J have a  
 560  $\geq 90\%$  probability of occurrence over the main localities. These joint obser-  
 561 vations suggest that for the case of Vulcano, the proximity to the active vent  
 562 makes any VBP impact potentially critical for the built environment, reduc-  
 563 ing the need to consider various roof typologies or probabilities of occurrence.  
 564 This contrasts with the hazard related to tephra accumulation (Biass et al.,  
 565 2016).

566 Figure 9 and Table 5 summarize the impact of VBPs on the built envi-  
 567 ronment. Figure 9 can be read as a box and whisker plot, in which black  
 568 dots indicate raw composite probabilities of perforation of individual build-  
 569 ings ( $n = 1093$ ) calculated assuming typical roof typologies of Spence et al.  
 570 (2005) (x axis). The resulting distributions are displayed as the median (red

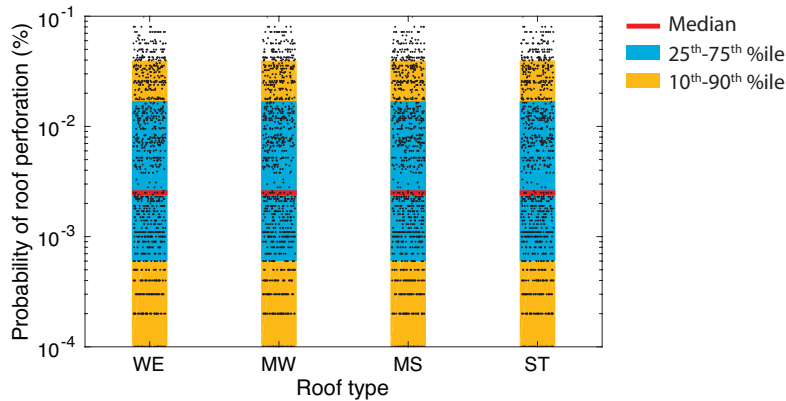


Figure 9: Impact on the built environment expressed as a probability of roof perforation (y axis) for the various roof types of Spence et al. (2005). Black dots show the probability of roof collapse of each building assuming a given roof typology of Spence et al. (2005) (x axis). Distributions of probabilities over all buildings are summarized as the median (red line), the 25<sup>th</sup>–75<sup>th</sup> interval (blue box) and the 10<sup>th</sup>–90<sup>th</sup> interval (orange box). For visibility, the lower y axis was manually set to  $10^{-4}\%$ .

571 line), the 25<sup>th</sup>–75<sup>th</sup> percentiles range (blue area) and the 10<sup>th</sup>–90<sup>th</sup> percentiles  
 572 range (orange area). Figure 9 shows how 90% of the building stock of Vul-  
 573 cano (i.e. 90<sup>th</sup> percentile) has a probability of  $\leq 4 \times 10^{-2}\%$  of roof perforation  
 574 by VBP impact, regardless of the building type. Table 5 reports the same  
 575 information.

## 576 6. Discussion

577 We introduce a new model called *The Great Balls of Fire* designed for the  
 578 probabilistic analysis of VBP impacts. The model relies on the identification  
 579 of probabilistic eruption scenarios described by distributions of selected in-  
 580 put parameters, namely i) initial ejection velocities, ii) size distribution and  
 581 iii) densities of VBPs. Sets of post-processing functions are also provided  
 582 to compile probabilities of VBP impacts exceeding hazardous thresholds of  
 583 kinetic energies. Probabilities can be expressed on a pixel-based approach,  
 584 suitable for hazard and pre-event impact assessments, or on zones of interests  
 585 (either concentric circles around or radial sector around the vent), suitable  
 586 for hazard zoning purposes.



Table 5: Final pre-event impact assessment showing the probability of roof perforation calculated at given percentiles on the distributions shown in Fig. 9. For instance, the 10<sup>th</sup> percentile shows that 10% of the building stock has a  $\leq 1.0 \times 10^{-4}\%$  probability of roof perforation.

Percentile	Probability (%)
10 <sup>th</sup>	$1.0 \times 10^{-4}$
25 <sup>th</sup>	$6.0 \times 10^{-4}$
50 <sup>th</sup>	$2.5 \times 10^{-3}$
75 <sup>th</sup>	$1.7 \times 10^{-2}$
90 <sup>th</sup>	$4.0 \times 10^{-2}$

587 *6.1. Probabilistic hazard assessment for VBPs*

588 Hazard assessments for VBPs published in the literature follow two main  
589 approaches. Some authors used the *Eject!* model to estimate probability  
590 density functions of impact distances based on ESPs inferred from observed  
591 VBPs (e.g. Sandri et al., 2014). In contrast, other authors associate hazard  
592 zones based on deterministic eruption scenarios with their respective proba-  
593 bilities of occurrence (e.g. Alatorre-Ibargüengoitia et al., 2006, 2012). Here,  
594 we aim at providing a fully probabilistic assessment for VBP impacts as a ba-  
595 sis to produce long-term multi-hazard assessments based on Bayesian event  
596 trees (e.g. Marzocchi et al., 2008; Selva et al., 2010; Sandri et al., 2014; Shel-  
597 drake, 2014; Thompson et al., 2015). The probabilistic approach adopted  
598 here is associated with a dependency on both the number of simulated VBPs  
599 and on the size of the zones of interest defined to average VBP impacts.  
600 This aspect should be investigated on a case-per-case basis, with the aim of  
601 finding the best compromise between computation time and output accuracy.  
602 For the example of La Fossa, Figure 3 shows minimum discrepancies of mean  
603 and standard deviation values of probabilities from  $10^6$  simulated particles,  
604 which generates valid results up to a distance 3,000 m away from the vent,  
605 shown as the dashed circle on Figure 6. In contrast,  $10^7$  particles increase  
606 the confidence radius to about 3,500 m, but results in both calculation and  
607 post-processing times multiplied by a factor 10.

608 *6.2. Probabilistic eruption scenarios for VBPs*

609 In probabilistic hazard assessments, eruption scenarios are typically ex-  
610 pressed as distributions of the most critical ESPs for the modelled phe-  
611 nomenon (e.g. earthquake source parameters for seismic and tsunami hazard

612 assessments, Geist and Parsons, 2006; volume for landslide hazard assess-  
613 ments, Guzzetti et al., 2005; thickness and volumes for lava flows, Connor  
614 et al., 2012). Alatorre-Ibargüengoitia et al. (2006) identified the total kinetic  
615 energy of Vulcanian explosions as the relevant ESP for defining eruption sce-  
616 narios for VBPs, which can practically only be relevant when i) the ballistic  
617 model is coupled with a conduit model (e.g. Alatorre-Ibargüengoitia et al.,  
618 2012) and ii) when deterministic eruption scenarios are used.

619 Eruption scenarios as defined with our method differ from those pre-  
620 sented by Alatorre-Ibargüengoitia et al. (2012) for Popocatepetl on two main  
621 points. Firstly, in our method, ESPs are those identified by Mastin (2001),  
622 stochastically sampled on either Gaussian or uniform distributions (Table 3).  
623 Secondly, the hazard zones resulting from the hazard assessment of Alatorre-  
624 Ibargüengoitia et al. (2012) for Popocatepetl are a direct consequence of the  
625 eruption scenarios, and, for instance, the high-hazard zone is defined as the  
626 typical range reached by VBPs resulting from the most likely and least in-  
627 tense type of activity. This deterministic approach, although complementary  
628 to the probabilistic approach when the probability of a future eruption tends  
629 to 1 (Marzocchi et al., 2008), is of limited information for long-term planning  
630 and risk reduction strategies. As an example, the cone of Popocatepetl is  
631 mostly deserted within a radius of a few kilometres around the vent, and the  
632 purpose of a risk assessment for VBPs is mainly the delimitation of exclusion  
633 zones. In contrast, urban areas are found within a radius of 1 *km* around La  
634 Fossa and probabilistic approaches become a necessity to estimate the likeli-  
635 hood of occurrence of VBPs impacts as a first step towards the development  
636 and implementation of pro-active risk mitigation strategies.

### 637 *6.3. Eruptive scenarios at La Fossa*

638 We developed a scenario for typical long-lasting Vulcanian eruptions at  
639 La Fossa based on the inversion of field observations (Fig. 2) and the com-  
640 parison with published literature (e.g. Alatorre-Ibargüengoitia et al., 2012;  
641 Fitzgerald et al., 2014; Tsunematsu et al., 2014). Using the caprock assump-  
642 tion, VBPs of different sizes have equal probabilities to be launched in the  
643 velocity range expressed in Table 3. Ejection velocities reported in the liter-  
644 ature range from 30 to 400  $\text{m}\cdot\text{s}^{-1}$  (Fagents and Wilson, 1993; Mastin, 1995;  
645 Wright et al., 2007; Feeley and Winer, 2009; Alatorre-Ibargüengoitia et al.,  
646 2012; Fitzgerald et al., 2014). In the case of La Fossa, the distribution was  
647 assumed Gaussian with values of mean and standard deviations of 100 and  
648 50  $\text{m}\cdot\text{s}^{-1}$ , respectively, which implies that 95% of the VBP's will result in

649 ejection velocities comprised between  $>0$  and  $200 \text{ m}\cdot\text{s}^{-1}$ , respectively. We ar-  
650 gue that this range is justifiable because i) it covers the majority of ejection  
651 velocities identified for other volcanoes while discarding sub- or supersonic  
652 velocities that are unlikely at La Fossa and ii) agrees with ranges obtained  
653 through inversion of field data (Fig. 2). The size distribution of VBPs is  
654 described here by a Gaussian distribution in  $\phi$  units (i.e. a log-normal dis-  
655 tribution is metres).

656 At La Fossa, the 1888–1890 eruption is characterized by at least three  
657 populations of VBPs characterized by different densities (Table 2). Our ap-  
658 proach accounts for three different populations of densities, weighing the  
659 number of simulated VBP according to proportions of occurrence of each  
660 VBP type observed in the field. However, observations of Mercalli and Sil-  
661 vestri (1891) suggest that each VBP type was produced at different stages of  
662 the two-year-long Vulcanian cycle. Outcomes of our probabilistic hazard as-  
663 sessment do not capture the evolution of VBP type through time and should  
664 be viewed as a time-integrated hazard over the duration of a Vulcanian cycle.

#### 665 6.4. VBP hazard for Vulcano

666 At La Fossa, Figure 6A–B shows suggests that all VBPs are likely to  
667 exceed energies critical for the strongest building typology. Energies of 60  
668 J and 8,000 J have maximum probabilities of occurrence of 17% and 11%,  
669 respectively, and a minimum probability of  $10^{-4}\%$  (Fig. 6) is constrained by  
670 the number of simulated particles and occurs when a given pixel was impacted  
671 by one single VBP. Such low probabilities are a consequence of the VBP  
672 hazard occurring on discrete points, which contrasts with the continuous  
673 blanketing caused by tephra fallout. For tephra fallout, a probability of  
674 100% occurs in a given pixel when all simulated eruptions result in deposits  
675 exceeding a critical threshold of tephra accumulation. In contrast, when  
676 considering VBPs, an hypothetical probability of 100% would imply that all  
677 simulated particles fell into a single pixel with energies exceeding a critical  
678 energy threshold. As a result, although Biass et al. (2016) show an average  
679 probability 15–30% to exceed critical accumulations of tephra for the collapse  
680 of the weakest roofs in the Porto area, probabilities of occurrences of VBPs  
681 with critical energies for the built environment are of about  $10^{-2}\%$ . When  
682 probability maps are converted to energy maps (Fig. 6), our results show a  
683 probability of occurrence of high energies increasing with distance from the  
684 vent. For the case of a steam-blast eruption, Dellino et al. (2011) suggest  
685 a zone of maximum energy of  $10^6$  J extending 200 m from the vent. Our

686 probabilistic approach suggests that in the case of a Vulcanian eruption,  
687 such an energy has a 90% probability to be exceeded within a radius of 3000  
688 m around the vent.

689 The southern flank of the 391 m–high cone of La Fossa is surrounded by  
690 a caldera rim rising from 250 to 400 m a.s.l. From the DEM, the height  
691 of the actual crater was estimated at  $\sim 220$  m, and GBF simulations were  
692 performed with a 200 m–high region of reduced drag (Table 3). As a result,  
693 although Figure 7 reveals a slight increase of probabilities towards NNE, our  
694 hazard assessment shows that the island does not host significant topographic  
695 barriers to shelter from VBPs, leaving only the southernmost part of the  
696 island with a virtually null probability of impact. On the other hand, the  
697 close proximity of the studied area to the source vent greatly reduces the  
698 influence of the radius of reduced drag on the final probabilities.

699 Biass et al. (2016) presents a study of wind patterns for the period 1980–  
700 2010 inferred from the ECMWF ERA- Interim database (Dee et al., 2011),  
701 which reveals a  $\sim 70\%$  probability of wind directed towards SE at sea level,  
702 with associated velocities rarely higher than  $20 \text{ m s}^{-1}$ . To test the influence of  
703 wind on the final probabilistic hazard assessment, simulations were run with a  
704 mean wind with a constant velocity of  $20 \text{ m s}^{-1}$  and a constant wind direction  
705 (i.e. provenance +  $180^\circ$ ) of  $135^\circ$ . Results show that the final probabilities are  
706 not significantly affected by wind conditions. This is due on one side to the  
707 fact that smaller particles will be more influenced by wind forces, which will  
708 necessarily fall relatively close to the vent due to the caprock assumption. In  
709 this case the large number of particles falling in proximal area is the dominant  
710 influence on the final probability values. On the other side, only a limited  
711 number of large particles will impact more distal areas, but since wind has  
712 little effect on them, their additional displacement is not sufficient to affect  
713 the final probability values.

#### 714 *6.5. Pre–event impact assessment*

715 In our impact assessment, the physical vulnerability only describes the  
716 likelihood of roof perforation resulting from a dynamic impact. This im-  
717 plies that the risk considered here regards a potential loss of life (e.g. Spence  
718 et al., 2005; Jenkins et al., 2014) rather than expressing the loss of economical  
719 value (e.g. Blong, 2003a). A comprehensive impact assessment on the built  
720 environment should include not only roof perforation but also aspects such  
721 as structure collapse and impacts on walls. Additionally, our analysis does  
722 not consider the physical impact on lifelines, nor attempts to quantify the

723 systemic repercussions of the physical impact on critical infrastructures identified in Figure 1. Nevertheless, this work is a first steps towards a holistic  
724 risk assessment that systematically includes a component of impact within  
725 probabilistic studies of the volcanic hazards.  
726

727 Following Biass et al. (2016), the vulnerability of the built environment  
728 was based on the typical building types of Spence et al. (2005), extrapolated  
729 to dynamic impacts following two main assumptions. Firstly, the limited  
730 observations of damages related to VBPs impacts does not allow to develop  
731 robust vulnerability curves. In natural hazards, the closest analogous phenomena associated with impacts at high kinetic energies include hail storms  
732 and rockfalls (e.g. Andrews and Blong, 1997; Hohl et al., 2002; Agliardi et al.,  
733 2009; Mavrouli and Corominas, 2010a,b). Resulting vulnerability curves can  
734 take various shapes such as sigmoid (e.g. Agliardi et al., 2009) and logistic  
735 (e.g. Hohl et al., 2002) shapes. Here, in the absence of more detailed information, we follow the approach undertaken for tephra fallout (e.g. Pomonis  
736 et al., 1999; Spence et al., 2005; Jenkins et al., 2014) using a lognormal  
737 distribution and a fixed coefficient of variation of 0.2. Secondly, published  
738 post-event impact assessments report VBP impacts associated with variable  
739 energy thresholds (e.g. Blong, 1984; Pomonis et al., 1999; Blong, 2003b).  
740 Here, we estimated mean energy thresholds for the built environment on  
741 Vulcano by comparing observed impacts with typology of buildings resulting  
742 from our field survey (Biass et al., 2016). As a result, two end-members of  
743 vulnerability to VBPs were identified comprising tile roofs on the weakest  
744 spectrum and reinforced concrete roofs on the strongest. Figure 4 reflects  
745 this bipolarity due to critical energy thresholds varying by orders of magnitude  
746 between the two families of roofs identified in Vulcano (i.e. tiles and  
747 reinforced concrete; Table 4). However, due to the proximity of the built environment  
748 to the eruptive vent, there is an equally high probability of impact  
749 at Vulcano regardless of the roof type.  
750

751 In terms of cascading effects between volcanic hazards, the relationship  
752 between VBPs and tephra is ambiguous. On one hand, tephra can act as a  
753 blanket absorbing energy from a VBP and thus reduce its propensity to perforation  
754 from a dynamic impact. On another hand, VBPs can increase the static load  
755 already caused by tephra layers and contribute to roof collapse.  
756 These complex vulnerability patterns occurring in the context of multi-hazards  
757 risk assessments were already discussed by Zuccaro et al. (2008)  
758 and underline the complex task of combining vulnerability curves for different  
759 natures of hazards (i.e. static load vs. dynamic impact) potentially  
760

761 simultaneously affecting exposed elements.

## 762 **7. Conclusion**

763 A new approach for the hazard assessment related to the ejection of VBPs  
764 is introduced, which quantifies the probabilities of occurrence of VBP impacts  
765 exceeding hazardous thresholds of kinetic energy. This approach, in line with  
766 recent efforts to quantify volcanic hazards in terms of probabilities, relies on  
767 a new ballistic model called *The Great Balls of Fire*, with the main features  
768 being:

- 769 • The definition of ESPs in terms of probability distributions;
- 770 • A variable drag coefficient;
- 771 • A fast computation time;
- 772 • The possibility to work on single CPUs or clusters of computers;
- 773 • Platform independent.

774 The model is distributed under a GPL3 and is available on *GitHub* (<https://github.com/paradigm>)  
775 along with post-processing functions and the user manual. It was validated  
776 using field observations of VBPs associated with the 1888–1890 eruption of  
777 La Fossa volcano. Additionally, sets of *Matlab* functions are provided to post  
778 process the model output into probabilistic hazard assessments for VBPs,  
779 resulting in a format useful for the integration in various GIS environments.

780 A generic Vulcanian eruption scenario was identified for La Fossa based  
781 on the stratigraphy of the last 1000 years. Results show that the settlements  
782 of Lentia and Porto are the most likely to be impacted by VBP, whereas  
783 Vulcanello and Piano are relatively safer (Fig. 4). In addition, the vulner-  
784 ability of the built environment was assessed by extrapolating the generic  
785 tephra fallout vulnerability curves for European roofs of Spence et al. (2005)  
786 to the impact of VBPs based on a review of critical energy thresholds found  
787 in the literature along with a field survey of the built environment on Vul-  
788 cano. Both hazard and vulnerability aspects were then combined to produce  
789 a first-order pre-event impact assessment in terms of potential number of  
790 affected buildings. Results show a high vulnerability of the built environ-  
791 ment to the VBP hazard, and half of the building stock has a  $\geq 2.5 \times 10^{-3}\%$   
792 probability of roof perforation.

793 **Acknowledgements**

794 We are grateful to C. Frischknecht, H. Monnard, A. Cuomo and I. Manzella  
795 for providing the results of the building survey, to A. Galderisi for the building  
796 shapefiles, to L. Chevalley et C. Haenggeli for their help in the characteri-  
797 zation of the built environment, to G. Bagheri, S. Jenkins and L. Pioli for  
798 the insightful comments and to J.L. Lewis for a great name. Computations  
799 were performed at University of Geneva on the Baobab cluster. S. Biass is  
800 supported by a SNF grant (#200021-129997).

801 Agliardi, F., Crosta, G.B., Frattini, P., 2009. Integrating rockfall risk as-  
802 sessment and countermeasure design by 3D modelling techniques. *Nat.*  
803 *Hazards Earth Syst. Sci.* 9, 1059–1073. doi:10.5194/nhess-9-1059-2009.

804 Alatorre-Ibargüengoitia, M., Delgado-Granados, H., Dingwell, D., 2012. Haz-  
805 ard map for volcanic ballistic impacts at Popocatépetl volcano (Mexico).  
806 *Bull Volcanol* 74, 2155–2169.

807 Alatorre-Ibargüengoitia, M., Scheu, B., Dingwell, D., Delgado-Granados, H.,  
808 Taddeucci, J., 2010. Energy consumption by magmatic fragmentation and  
809 pyroclast ejection during Vulcanian eruptions. *Earth and Planetary Sci-*  
810 *ence Letters* 291, 60–69.

811 Alatorre-Ibargüengoitia, M.A., Delgado-Granados, H., 2006. Experi-  
812 mental determination of drag coefficient for volcanic materials: Cal-  
813 ibration and application of a model to Popocatépetl volcano (Mex-  
814 ico) ballistic projectiles. *Geophysical Research Letters* 33, L11302.  
815 doi:10.1029/2006GL026195.

816 Alatorre-Ibargüengoitia, M.A., Delgado-Granados, H., Farraz-Montes, I.A.,  
817 2006. Hazard zoning for ballistic impact during volcanic explosions at Vol-  
818 cán de Fuego de Colima (México). *Geological Society of America Special*  
819 *Papers* 402, 209–216.

820 Andrews, K., Blong, R., 1997. March 1990 Hailstorm Damage in Sydney,  
821 Australia. *Natural Hazards* 16, 113–125. doi:10.1023/A:1007913508192.

822 Arrighi, S., Tanguy, J.C., Rosi, M., 2006. Eruptions of the last 2200 years  
823 at Vulcano and Vulcanello (Aeolian Islands, Italy) dated by high-accuracy  
824 archeomagnetism. *Physics of the Earth and Planetary Interiors* 159, 225–  
825 233.

- 826 Bianchi, L., 2007. L'eruzione 1888-1890 di Vulcano (Isole Eolie): Analisi  
827 stratigrafica, fisica e composizionale dei prodotti. Unpublished msc thesis.  
828 Università di Pisa.
- 829 Biass, S., Bonadonna, C., Traglia, F., Pistolesi, M., Rosi, M., Lestuzzi, P.,  
830 2016. Probabilistic evaluation of the physical impact of future tephra  
831 fallout events for the Island of Vulcano, Italy. *Bulletin of Volcanology*  
832 78, 1–22. doi:10.1007/s00445-016-1028-1.
- 833 Biass, S., Scaini, C., Bonadonna, C., Folch, A., Smith, K., Höskuldsson, A.,  
834 2014. A multi-scale risk assessment for tephra fallout and airborne con-  
835 centration from multiple Icelandic volcanoes - Part 1: Hazard assessment.  
836 *Nat. Hazards Earth Syst. Sci.* 14, 2265–2287. doi:10.5194/nhess-14-2265-  
837 2014.
- 838 Blong, R., 2003a. A New Damage Index. *Nat. Hazards.* 30, 1–23.
- 839 Blong, R., 2003b. Building damage in Rabaul, Papua New Guinea, 1994.  
840 *Bulletin of Volcanology* 65, 43–54.
- 841 Blong, R.J., 1984. *Volcanic hazards. A sourcebook on the effects of eruptions.*  
842 Academic Press, Orlando.
- 843 Bonadonna, C., 2006. Probabilistic modelling of tephra dispersion, in:  
844 Mader, H.M., Coles, S.G., Connor, C.B., Connor, L.J. (Eds.), *Statistics in*  
845 *volcanology.* Geological Society of London, London, pp. 243–259.
- 846 Bonadonna, C., Biass, S., Manzella, I., Galderisi, A., Ceudech, A., Ferrara,  
847 F., Delmonaco, G., Menoni, S., Minucci, G., Belvaux, M., Manceau, J.,  
848 Montfort-Climent, D., Sabourault, P., Foerster, E., 2011. Application of  
849 an integrated vulnerability conceptual approachm Del. 5.3.3: Development  
850 of the Integrated Approach on the Vulcano case study. Tech. Rep. 212045,  
851 Ensure project. Technical Report. ENSURE Project.
- 852 Connor, L., Connor, C., Meliksetian, K., Savov, I., 2012. Probabilistic ap-  
853 proach to modeling lava flow inundation: a lava flow hazard assessment  
854 for a nuclear facility in Armenia. *J Appl. Volcanol.* 1, 1–19.
- 855 De Astis, G., Lucchi, F., Dellino, P., La Volpe, L., Tranne, C.A., Frezzotti,  
856 M.L., Peccerillo, A., 2013. Geology, volcanic history and petrology of Vul-  
857 cano (central Aeolian archipelago). *Geological Society, London, Memoirs*  
858 37, 281–349. doi:10.1144/M37.11.



- 859 De Astis, G., Volpe, L., Peccerillo, A., Civetta, L., 1997. Volcanological and  
860 petrological evolution of Vulcano island (Aeolian Arc, southern Tyrrhenian  
861 Sea). *Journal of Geophysical Research: Solid Earth* 102, 8021–8050.
- 862 De Fiore, O., 1922. Vulcano (Isole Eolie), in: Friedlaender, I. (Ed.), *Revisita*  
863 *Vulcanologica* (Suppl. 3), pp. 1–393.
- 864 De' Michieli Vitturi, M., Neri, A., Esposti Ongaro, T., Lo Savio, S., Boschi,  
865 E., 2010. Lagrangian modeling of large volcanic particles: Application to  
866 Vulcanian explosions. *Journal of Geophysical Research: Solid Earth* 115,  
867 B08206. doi:10.1029/2009JB007111.
- 868 Dee, D.P., Uppala, S.M., Simmons, A.J., Berrisford, P., Poli, P., Kobayashi,  
869 S., Andrae, U., Balmaseda, M.A., Balsamo, G., Bauer, P., Bechtold, P.,  
870 Beljaars, A.C.M., van de Berg, L., Bidlot, J., Bormann, N., Delsol, C., Dra-  
871 gani, R., Fuentes, M., Geer, A.J., Haimberger, L., Healy, S.B., Hersbach,  
872 H., Hólm, E.V., Isaksen, I., Kållberg, P., Köhler, M., Matricardi, M., Mc-  
873 Nally, A.P., Monge-Sanz, B.M., Morcrette, J.J., Park, B.K., Peubey, C.,  
874 de Rosnay, P., Tavolato, C., Thépaut, J.N., Vitart, F., 2011. The ERA-  
875 Interim reanalysis: configuration and performance of the data assimilation  
876 system. *Quarterly Journal of the Royal Meteorological Society* 137, 553–  
877 597. doi:10.1002/qj.828.
- 878 Dellino, P., Astis, G., Volpe, L., Mele, D., Sulpizio, R., 2011. Quantita-  
879 tive hazard assessment of phreatomagmatic eruptions at Vulcano (Aeo-  
880 lian Islands, Southern Italy) as obtained by combining stratigraphy, event  
881 statistics and physical modelling. *Journal of Volcanology and Geothermal*  
882 *Research* 201, 364–384.
- 883 Dellino, P., La Volpe, L., 1997. Stratigrafia, dinamiche eruttive e deposizion-  
884 ali, scenario eruttivo e valutazioni di pericolosità a La Fossa di Vulcano.  
885 Technical Report. CNR-Gruppo Nazionale per la Vulcanologia, Volume  
886 speciale Vulcano-Progetto triennale 1993–1995.
- 887 Di Traglia, F., 2011. The last 1000 years of eruptive activity at the Fossa  
888 Cone (Island of Vulcano, Southern Italy). Ph.D. thesis. Università di Pisa.
- 889 Di Traglia, F., Pistolesi, M., Rosi, M., Bonadonna, C., Fusillo, R., Roverato,  
890 M., 2013. Growth and erosion: The volcanic geology and morphological

- 891 evolution of La Fossa (Island of Vulcano, Southern Italy) in the last 1000  
892 years. *Geomorphology* 194, 94–107. doi:10.1016/j.geomorph.2013.04.018.
- 893 Druitt, T.H., Young, S.R., Baptie, B., Bonadonna, C., Calder, E.S., Clarke,  
894 A.B., Cole, P.D., Harford, C.L., Herd, R.A., Luckett, R., Ryan, G., Voight,  
895 B., 2002. Episodes of cyclic Vulcanian explosive activity with fountain col-  
896 lapse at Soufrière Hills Volcano, Montserrat, in: Druitt, T., Kokelaar, B.  
897 (Eds.), *The eruption of Soufrière Hills Volcano, Montserrat, from 1995 to*  
898 *1999*. Geological Society of London, London. volume 21, pp. 281–306. URL:  
899 <http://mem.lyellcollection.org/content/21/1/281.abstract>,  
900 doi:10.1144/GSL.MEM.2002.021.01.13.
- 901 Fagents, S.A., Wilson, L., 1993. Explosive volcanic eruptions—VII. The  
902 ranges of pyroclasts ejected in transient volcanic explosions. *Geophysical*  
903 *Journal International* 113, 359–370.
- 904 Feeley, T.C., Winer, G.S., 2009. Volcano hazards and potential risks on St.  
905 Paul Island, Pribilof Islands, Bering Sea, Alaska. *Journal of Volcanology*  
906 *and Geothermal Research* 182, 57–66.
- 907 Fitzgerald, R., Tsunematsu, K., Kennedy, B., Breard, E., Lube, G., Wilson,  
908 T., Jolly, A., Pawson, J., Rosenberg, M., Cronin, S., 2014. The application  
909 of a calibrated 3D ballistic trajectory model to ballistic hazard assessments  
910 at Upper Te Maari, Tongariro. *Journal of Volcanology and Geothermal*  
911 *Research* doi:10.1016/j.jvolgeores.2014.04.006.
- 912 Fournier d’Albe, E.M., 1979. Objectives of volcanic monitoring and predic-  
913 tion. *J Geol Soc Lond* 136, 321–326.
- 914 Frazzetta, G., Gillot, P.Y., Volpe, L., Sheridan, M.F., 1984. Volcanic haz-  
915 ards at Fossa of Vulcano: Data from the last 6,000 years. *Bulletin Vol-*  
916 *canologique* 47, 105–124. doi:10.1007/BF01960543.
- 917 Frazzetta, G., La Volpe, L., Sheridan, M.F., 1983. Evolution of the Fossa  
918 Cone, Vulcano. *Journal of Volcanology and Geothermal Research* 17, 329–  
919 360. doi:10.1016/0377-0273(83)90075-6.
- 920 Fudali, R.F., Melson, W.G., 1971. Ejecta velocities, magma chamber pressure  
921 and kinetic energy associated with the 1968 eruption of Arenal volcano.  
922 *Bulletin Volcanologique* 35, 383–401. doi:10.1007/BF02596963.

- 923 Geist, E.L., Parsons, T., 2006. Probabilistic analysis of tsunami hazards.  
924 *Natural Hazards* 37, 277–314.
- 925 Gioncada, A., Mazzuoli, R., Bisson, M., Pareschi, M., 2003. Petrology of vol-  
926 canic products younger than 42 ka on the Lipari–Vulcano complex (Aeolian  
927 Islands, Italy): an example of volcanism controlled by tectonics. *Journal of*  
928 *Volcanology and Geothermal Research* 122, 191–220. doi:10.1016/S0377-  
929 0273(02)00502-4.
- 930 Gonzalez, F.I., Geist, E.L., Jaffe, B., Kanoglu, U., Mofjeld, H., Synolakis,  
931 C.E., Titov, V.V., Arcas, D., Bellomo, D., Carlton, D., Horning, T., John-  
932 son, J., Newman, J., Parsons, T., Peters, R., Peterson, C., Priest, G.,  
933 Venturato, A., Weber, J., Wong, F., Yalciner, A., 2009. Probabilistic  
934 tsunami hazard assessment at Seaside, Oregon, for near- and far-field seis-  
935 mic sources. *Journal of Geophysical Research-Oceans* 114.
- 936 Gurioli, L., Zanella, E., Gioncada, A., Sbrana, A., 2012. The historic  
937 magmatic-hydrothermal eruption of the Breccia di Commenda, Vulcano,  
938 Italy. *Bulletin of Volcanology* , 1–20.
- 939 Guzzetti, F., Reichenbach, P., Cardinali, M., Galli, M., Ardizzone, F., 2005.  
940 Probabilistic landslide hazard assessment at the basin scale. *Geomorphol-*  
941 *ogy* 72, 272–299. doi:10.1016/j.geomorph.2005.06.002.
- 942 Heneka, P., Hofherr, T., 2011. Probabilistic winter storm risk assess-  
943 ment for residential buildings in Germany. *Natural Hazards* 56, 815–831.  
944 doi:10.1007/s11069-010-9593-7.
- 945 Hohl, R., Schiesser, H.H., Aller, D., 2002. Hailfall: the relationship between  
946 radar-derived hail kinetic energy and hail damage to buildings. *Atmo-*  
947 *spheric Research* 63, 177–207. doi:10.1016/S0169-8095(02)00059-5.
- 948 ISTAT, 2005. Progetto Census 2000 - Aggiornamento delle basi territoriali,  
949 Descrizione dei dati. Technical Report.
- 950 Jenkins, S., Magill, C., McAneney, J., Blong, R., 2012. Regional ash fall  
951 hazard I: a probabilistic assessment methodology. *Bulletin of Volcanology*  
952 , 1–14.

- 953 Jenkins, S., Spence, R., Fonseca, J., Solidum, R., Wilson, T., 2014. Volcanic  
954 risk assessment: Quantifying physical vulnerability in the built environ-  
955 ment. *Journal of Volcanology and Geothermal Research* 276, 105–120.  
956 doi:10.1016/j.jvolgeores.2014.03.002.
- 957 Kaneko, T., Maeno, F., Nakada, S., 2016. 2014 Mount Ontake eruption:  
958 characteristics of the phreatic eruption as inferred from aerial observations.  
959 *Earth, Planets and Space* 68, 1–11. doi:10.1186/s40623-016-0452-y.
- 960 Keller, J., 1980. The island of Vulcano. *Rendiconti Società Italiana Miner-  
961 alogia e Petrologia* 36, 369–414.
- 962 Maeno, F., Nakada, S., Nagai, M., Kozono, T., 2013. Ballistic ejecta and  
963 eruption condition of the vulcanian explosion of Shinmoedake volcano,  
964 Kyushu, Japan on 1 February, 2011. *Earth, Planets and Space* 65, 609–  
965 621. doi:10.5047/eps.2013.03.004.
- 966 Marzocchi, W., Sandri, L., Selva, J., 2008. BET\_EF: a probabilistic tool  
967 for long- and short-term eruption forecasting. *Bulletin of Volcanology* 70,  
968 623–632.
- 969 Mastin, L.G., 1995. Thermodynamics of gas and steam-blast eruptions. *Bul-  
970 letin of Volcanology* 57, 85–98. doi:10.1007/BF00301399.
- 971 Mastin, L.G., 2001. A simple calculator of ballistic trajecto-  
972 ries for blocks ejected during volcanic eruptions. Technical Re-  
973 port. U.S. Geological Survey Open-File Report 01-45. URL:  
974 <http://pubs.usgs.gov/of/2001/0045/>.
- 975 Mavrouli, O., Corominas, J., 2010a. Rockfall vulnerability assessment for  
976 reinforced concrete buildings. *Nat. Hazards Earth Syst. Sci.* 10, 2055–  
977 2066. doi:10.5194/nhess-10-2055-2010.
- 978 Mavrouli, O., Corominas, J., 2010b. Vulnerability of simple reinforced  
979 concrete buildings to damage by rockfalls. *Landslides* 7, 169–180.  
980 doi:10.1007/s10346-010-0200-5.
- 981 Mendoza-Rosas, A.T., De la Cruz-Reyna, S., 2008. A statistical method  
982 linking geological and historical eruption time series for volcanic hazard  
983 estimations: Applications to active polygenetic volcanoes. *Journal of Vol-  
984 canology and Geothermal Research* 176, 277–290.

- 985 Mercalli, G., Silvestri, O., 1891. Le eruzioni dell'Isola di Vulcano incominciate  
986 il 3 agosto 1888 e terminate il 22 marzo 1890, relazione scientifica. Ann  
987 Ufficio Centrale Metereol Geodin Ital 10, 1–213.
- 988 Minakami, T., 1942. 5. On the Distribution of Volcanic Ejecta. (Part 1)  
989 The Distributions of Volcanic Bombs ejected by the Recent Explosion of  
990 Asama. Bulletin of the Earthquake Research Institute 20.
- 991 Petrazzuoli, S., Zuccaro, G., 2004. Structural resistance of reinforced concrete  
992 buildings under pyroclastic flows: a study of the Vesuvian area. Journal of  
993 Volcanology and Geothermal Research 133, 353–367. doi:10.1016/S0377-  
994 0273(03)00407-4.
- 995 Pistolesi, M., Donne, D., Pioli, L., Rosi, M., Ripepe, M., 2011. The 15  
996 March 2007 explosive crisis at Stromboli volcano, Italy: Assessing physical  
997 parameters through a multidisciplinary approach. Journal of Geophysical  
998 Research 116.
- 999 Pomonis, A., Spence, R., Baxter, P., 1999. Risk assessment of residential  
1000 buildings for an eruption of Furnas Volcano, Sao Miguel, the Azores. Jour-  
1001 nal of volcanology and geothermal research 92, 107–131.
- 1002 Rosi, M., Pistolesi, M., Bertagnini, A., Landi, P., Pompilio, M., Di Roberto,  
1003 A., 2013. Stromboli volcano, Aeolian Islands (Italy): present eruptive  
1004 activity and hazards. Geological Society, London, Memoirs 37, 473–490.  
1005 doi:10.1144/M37.14.
- 1006 Sandri, L., Thouret, J.C., Constantinescu, R., Biass, S., Tonini, R., 2014.  
1007 Long-term multi-hazard assessment for El Misti volcano (Peru). Bulletin  
1008 of Volcanology 76, 1–26. doi:10.1007/s00445-013-0771-9.
- 1009 Self, S., Wilson, L., Nairn, I., 1979. Vulcanian eruption mechanisms. Nature  
1010 277, 440–443.
- 1011 Selva, J., Costa, A., Marzocchi, W., Sandri, L., 2010. BET\_VH: exploring  
1012 the influence of natural uncertainties on long-term hazard from tephra  
1013 fallout at Campi Flegrei (Italy). Bulletin of Volcanology 72, 717–733.
- 1014 Sheldrake, T., 2014. Long-term forecasting of eruption hazards: a hierarchi-  
1015 cal approach to merge analogous eruptive histories. Journal of Volcanology  
1016 and Geothermal Research doi:10.1016/j.jvolgeores.2014.08.021.

- 1017 Spence, R.J.S., Kelman, I., Baxter, P.J., Zuccaro, G., Petrazzuoli, S., 2005.  
1018 Residential building and occupant vulnerability to tephra fall. *Natural*  
1019 *Hazards and Earth System Sciences* 5, 477–494.
- 1020 Steinberg, G.S., Lorenz, V., 1983. External ballistic of volcanic explosions.  
1021 *Bulletin Volcanologique* 46, 333–348. doi:10.1007/BF02597769.
- 1022 Thompson, M., Lindsay, J., Sandri, L., Biass, S., Bonadonna, C., Jolly,  
1023 G., Marzocchi, W., 2015. Exploring the influence of vent location and  
1024 eruption style on tephra fall hazard from the Okataina Volcanic Centre,  
1025 New Zealand. *Bulletin of Volcanology* 77, 1–23. doi:10.1007/s00445-015-  
1026 0926-y.
- 1027 Tsunematsu, K., 2012. New numerical solutions for the description of  
1028 volcanic particle dispersal. Ph.D. thesis. University of Geneva. URL:  
1029 <https://archive-ouverte.unige.ch/unige:26675>.
- 1030 Tsunematsu, K., Chopard, B., Falcone, J.L., Bonadonna, C., 2014. A nu-  
1031 merical model of ballistic transport with collisions in a volcanic setting.  
1032 *Computers & Geosciences* 63, 62–69. doi:10.1016/j.cageo.2013.10.016.
- 1033 Vanderkluysen, L., Harris, A., Kelfoun, K., Bonadonna, C., Ripepe, M., 2012.  
1034 Bombs behaving badly: unexpected trajectories and cooling of volcanic  
1035 projectiles. *Bulletin of Volcanology* 74, 1849–1858. doi:10.1007/s00445-  
1036 012-0635-8.
- 1037 Wilson, L., 1972. Explosive Volcanic Eruptions-II The Atmospheric Tra-  
1038 jectories of Pyroclasts. *Geophysical Journal International* 30, 381–392.  
1039 doi:10.1111/j.1365-246X.1972.tb05822.x.
- 1040 Wilson, L., 1980. Relationships between pressure, volatile content and ejecta  
1041 velocity in three types of volcanic explosion. *Journal of Volcanology and*  
1042 *Geothermal Research* 8, 297–313. doi:10.1016/0377-0273(80)90110-9.
- 1043 Wilson, T., Stewart, C., Sword-Daniels, V., 2011. Volcanic ash impacts on  
1044 critical infrastructure. *Phys. Chem. Earth Pt. A/B/C* .
- 1045 Wright, H., Cashman, K., Rosi, M., Cioni, R., 2007. Breadcrust bombs as  
1046 indicators of Vulcanian eruption dynamics at Guagua Pichincha volcano,  
1047 Ecuador. *Bulletin of Volcanology* 69, 281–300. doi:10.1007/s00445-006-  
1048 0073-6.

1049 Zanella, E., Astis, G., Lanza, R., 2001. Palaeomagnetism of welded,  
1050 pyroclastic-fall scoriae at Vulcano, Aeolian Archipelago. *Journal of Vol-*  
1051 *canology and Geothermal Research* 107, 71–86.

1052 Zuccaro, G., Cacace, F., Spence, R.J.S., Baxter, P.J., 2008. Impact of explo-  
1053 sive eruption scenarios at Vesuvius. *Journal of volcanology and geothermal*  
1054 *research* 178, 416–453.

1055